The Planetary Science Journal, 6:15 (24pp), 2025 January https://doi.org/10.3847/PSJ/ad9d42

Improved Constraints on the Vertical Profile of CH_4 at Jupiter's Mid- to High Latitudes, Using IRTF-TEXES and SOFIA-EXES Spectroscopy

James A. Sinclair[1], Thomas K. Greathouse[2], Rohini S. Giles[2], Matthew Richter[3], Maisie Rashman[4], Curtis de Witt[5], Julianne Moses[5], Vincent Hue[6], Pablo Rodríguez-Ovalle[7], Thierry Fouchet[7], Ananyo Bhattacharya[8], Bilal Benmahi[9], Glenn S. Orton[1], Leigh N. Fletcher[10], and Patrick G. J. Irwin[11]

[1] Jet Propulsion Laboratory/California Institute of Technology, 4800 Oak Grove Drive, Pasadena, CA 91109, USA; james.sinclair@jpl.nasa.gov
[2] Southwest Research Institute, 6220 Culebra Road, San Antonio, TX 78238, USA
[3] Department of Physics and Astronomy, University of California Davis, 1 Shields Avenue, Davis, CA 95616, USA
[4] School of Physical Sciences, The Open University, Robert Hooke Building, Kents Hill, Milton Keynes, MK7 6AA, UK
[5] Space Science Institute, 4765 Walnut Street, STE B, Boulder, CO 80301, USA
[6] Aix-Marseille Université, Jardin du Pharo, 58 Boulevard Charles Livon, 13007 Marseille, France
[7] Observatoire de Paris, 77 Av. Denfert Rochereau, 75014 Paris, France
[8] Planetary Sciences Laboratory, University of Michigan, 1221 Beal Avenue, Ann Arbor, MI 48109, USA
[9] Université de Liège, STAR Institute, Quartier Agora - Bât. B5c, Allée du Six Août, 19CB-4000, Belgium
[10] School of Physics & Astronomy, University of Leicester, University Road, Leicester LE1 7RH, UK
[11] Department of Physics, University of Oxford, Clarendon Laboratory, Parks Road, Oxford, OX1 3PU, UK
Received 2024 July 29; revised 2024 November 30; accepted 2024 December 9; published 2025 January 20

Abstract

We present radiative transfer analyses of IRTF-TEXES and SOFIA-EXES mid-infrared spectra of Jupiter's mid- to high latitudes recorded between 2019 April 16 and 2023 July 20. The spectra were inverted across a photochemical model grid of varying eddy diffusion coefficient profiles, and the quality of fit of the synthetic spectra to the observed was used to constrain the CH_4 homopause level. For a subset of latitudes/dates, we find that the CH_4 homopause level is elevated in the region enclosed inside of, or magnetospherically poleward of, the northern ultraviolet main auroral emissions (MAEs) in comparison to the region outside or equatorward of the MAE. For example, using SOFIA-EXES results on 2021 June 10, we derived a CH_4 homopause level of $\log(p_H(\text{nbar})) = 1.54^{+0.51}_{-0.69}$ or $z_H = 453^{+128}_{-76}$ km above 1 bar poleward of the northern MAE at 68°N compared to a lower limit of $\log(p_H) > 2.43$ and upper limit of $z_H < 322$ km derived equatorward of the northern MAE. We therefore conclude that the region poleward of the northern MAE is, at times, subject to enhanced vertical transport resulting from auroral energy deposition. The exact mechanisms responsible for the enhanced vertical transport in Jupiter's auroral regions are uncertain: time-dependent circulation modeling of Jupiter's polar atmosphere is required to better understand this phenomenon. Poleward of the southern MAE, derived homopause levels agreed within uncertainty with those at equatorward locations. However, we consider this result a spatial sampling artifact rather than concluding that the southern auroral region is not subject to enhanced vertical transport.

Unified Astronomy Thesaurus concepts: Aurorae (2192); Planetary atmospheres (1244); Atmospheric dynamics (2300); Atmospheric composition (2120); Jupiter (873); Space weather (2037)

Materials only available in the online version of record: machine-readable table

1. Introduction

The polar atmosphere of Jupiter is significantly modulated by its external space environment. Magnetospheric dynamics driven by intrinsic magnetospheric processes (e.g., Io's volcanism) and by external solar wind perturbations ultimately drive electrons and ions into Jupiter's neutral atmosphere. The energy deposited manifests in emission over a large range of the electromagnetic spectrum, including the X-ray, ultraviolet, and infrared (e.g., T. Greathouse et al. 2021; R. E. Johnson et al. 2017; S. C. McEntee et al. 2023).

A significant amount of energy is deposited as deep as its middle atmosphere or stratosphere, thereby modifying its thermal structure, chemistry, and dynamics. Spatially, the majority of the heating is enclosed inside of the ultraviolet main auroral emissions (MAEs). This region inside of the ultraviolet MAEs is also described as being magnetospherically poleward of the MAEs. Vertically, auroral-related heating occurs at two levels of the atmosphere: at pressures lower than 0.1 mbar and at ~1 mbar. Thermospheric circulation modeling of Jupiter's polar atmosphere demonstrates that auroral heating dominates above 800 km (<0.1 μbar), Joule heating dominates down to 400 km (~1 μbar), and dynamical heating associated with ion drag dominates at pressures higher than 1 μbar (S. W. Bougher et al. 2005). The upper-stratospheric heating from 1 to 10 μbar sensed in mid-infrared observations would therefore be expected to be produced by some combination of Joule heating and ion drag. Dynamical heating associated with ion drag would be expected to be stronger closer to the MAE, where the velocity shears are strongest. Indeed, T. Cavalié et al. (2021) observed narrow, counterrotating jets in CO emission at ~0.1 mbar, which was coincident with the southern MAE and inferred to be circulation of neutrals driven by ion drag. Oddly, the warmest upper-stratospheric temperatures are generally observed in the polar region close to the magnetic pole (e.g., J. A. Sinclair et al. 2017b, 2018, 2019).

The exact source(s) of the lower-stratospheric heating are also uncertain. Thermospheric general circulation models (e.g., S. W. Bougher et al. 2005; J. Yates et al. 2014) have their lower boundary at several tens of microbars, and thus the dominant sources of heating at deeper pressures have not been predicted by circulation models. As noted above, T. Cavalié et al. (2021) observed a counterrotating vortex at 0.1 mbar, which was spatially coincident with the southern MAE. Such a circulation could drive downwelling, and therefore adiabatic heating at the deeper, 1 mbar levels, as suggested in J. A. Sinclair et al. (2023). However, a complication of this hypothesis is that it implies downwelling in contrast to the upward motions inferred from the elevated CH_4 homopause level poleward of the MAE (J. A. Sinclair et al. 2020; this work). Circulation modeling would be required to explore the viability of this mechanism as the source of the lower-stratospheric heating. Electrons with several hundred keV energies precipitate in Jupiter's atmosphere at ~0.1 mbar pressures (J. Gustin et al. 2016): electrons with several MeV energies would be required to precipitate and heat the atmosphere at ~1 mbar (A. Bhattacharya et al. 2025). While high fluxes of electrons with such energies are inferred/detected in Jupiter's external space environment (e.g., H. N. Becker et al. 2017; B. H. Mauk et al. 2018, 2020), these are generally detected coincident with Jupiter's MAE, and not the region poleward of the MAE where the majority of the 1 mbar heating is detected (e.g., J. A. Sinclair et al. 2017b, 2018). Nevertheless, recent measurements by Juno's Microwave Radiometer (MWR; M. A. Janssen et al. 2017) instrument reveal a potential layer of plasma absorption/reflection in the lower stratosphere and poleward of the MAE, which is inferred to be due to precipitation of MeV electrons (A. Bhattacharya et al., 2025). A further potential source of the lower-stratospheric heating may be the strong megavolt potentials detected over the region poleward of the MAE (e.g., G. Clark et al. 2017), which may be accelerating protons to the ~30 MeV required to precipitate at 1 mbar. The potential contribution of proton precipitation to the 1 mbar auroral-related heating will be the subject of future work (S. Houston et al. 2025, in preparation).

The energy deposited by auroral processes and the resulting heating has implications for the stratospheric dynamics. For example, the local maximum in temperature at ~1 mbar poleward of the MAE imposes a negative lapse rate at higher altitudes, which would allow upward transport by convection. Enhanced vertical transport in Jupiter's auroral regions, compared to elsewhere on the planet, was determined by C. D. Parkinson et al. (2006), who analyzed Cassini Ultraviolet Imaging Spectrometer (UVIS; L. W. Esposito et al. 2004) observations of Jupiter's helium airglow and determined that the eddy diffusion coefficient (the rate of atmospheric turbulence) at Jupiter's poles must be an order of magnitude higher than that derived at equatorial latitudes. Similarly, other studies inferred that the hydrocarbon homopause level, which is the level at which the eddy diffusion and molecular diffusion rates are equal and is a commonly used metric to quantify the rate of vertical transport, must be higher in the atmosphere at Jupiter's poles compared to elsewhere on the planet (J. Gustin et al. 2016; G. Clark et al. 2018). This result was partially confirmed in J. A. Sinclair et al. (2020), who performed a retrieval analysis of spectra from the Texas Echelon Cross Echelle Spectrograph on NASA's Infrared Telescope Facility (IRTF-TEXES; J. H. Lacy et al. 2002). The stratospheric emission features of the H_2 S(1) (hydrogen quadrupole), CH_3 (methyl radical), and CH_4 (methane) at ~587, ~606, and ~1248 cm^{-1}, respectively, were mapped across the planet. The spectra of all three features were inverted across a grid of photochemical models of varying eddy diffusion coefficient profiles, and thus homopause levels, and the quality of fit of the synthetic spectra to the observed was used to constrain the CH_4 homopause altitude (CHA) and uncertainty. CHAs derived using observations that sample latitudes/longitudes poleward of the northern ultraviolet MAEs were approximately 70–150 km higher compared to those derived from observations outside of or magnetospherically equatorward of the northern MAEs.

In this paper, we improve on the work detailed in J. A. Sinclair et al. (2020) in the following ways. First, in this work we present results from observations recorded on seven further nights between 2021 June 28 and 2023 July 20, in addition to the 2019 April 16 and 2019 August 20 measurements presented in J. A. Sinclair et al. (2020). This includes IRTF-TEXES observations and similar observations recorded by the Echelon Cross Echelle Spectrograph (EXES; M. J. Richter et al. 2018) on the Stratospheric Observatory for Infrared Astronomy (SOFIA; P. Temi et al. 2018). The additional observations are beneficial for better determining the extent of temporal variability of the homopause level. The data sets presented in J. A. Sinclair et al. (2020) also did not sufficiently sample longitudes poleward of the southern MAE, and thus the focus was on the northern auroral region. In this work, newer observations better sample the longitudes poleward of the southern MAE, which allows the homopause level in this region to be constrained. In addition, SOFIA-EXES observations sound higher levels in Jupiter's atmosphere, which reduced uncertainties on the CH_4 homopause level. Details on the IRTF-TEXES and SOFIA-EXES observations are provided in Sections 2 and 3, with individual observations used listed in Appendix A.

Second, we have improved the analysis to derive the location of the homopause. In this work, spectra are inverted over a grid of 13 models ranging in homopause pressure from 754 to 0.52 nbar and calculated at a latitude of 60°N, in contrast to J. A. Sinclair et al. (2020), where a grid of nine models from 295 to 0.52 nbar at a latitude of 30°N was used. Using a larger range in homopause pressure improves the constraint on the CH_4 homopause location and their uncertainties, and the use of the model results at 60°N is more appropriate given that this work focuses on Jupiter's mid- to high latitudes.

A third improvement in this work is that the statistical significance of spatial variations in the CH_4 homopause level is explored in both pressure and altitude units. In contrast, J. A. Sinclair et al. (2020) focused only on variations in the CH_4 homopause altitude. A difference in the rate of vertical transport between two locations can only be concluded if there is a statistically significant difference in homopause level in pressure space. Auroral-related heating, which is commonly observed poleward of the MAE (e.g., S. J. Kim et al. 1985; P. Drossart et al. 1993; J. A. Sinclair et al. 2017a, 2023), increases the atmospheric scale height such that a given pressure occurs at a higher altitude relative to a cooler location. A statistically significant difference in CH_4 homopause altitude poleward of the MAE compared to equatorward could result from enhanced vertical transport in the former, auroral-related heating in the former, or a combination of both. By determining the statistical significance of spatial variability of the CH_4

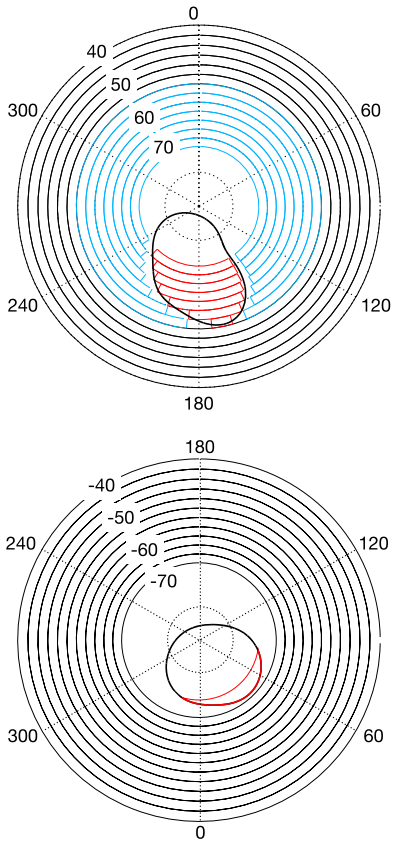

Figure 1. The latitude and longitude ranges used for coaddition of individual IRTF-TEXES spectra. Areas shown in black, blue, and red are henceforth described as the "longitudinal-mean," "non-auroral-mean," and "auroral-mean" observations, respectively. A similar scheme is adopted for SOFIA-EXES observations, but with a coarser latitude spacing. Spectra are not coadded at latitudes higher than ±74°, where diffraction blurs planet signal with dark sky.

homopause in both pressure and altitude space, we better determine whether there is indeed enhanced vertical transport poleward of the MAE or simply heating increasing the scale height of the atmosphere. The model grid, retrieval analysis, and methods for derivation of the CH_4 homopause level are given in Section 4.

2. IRTF-TEXES Observations

High-resolution ($65{,}000 < R < 80{,}000$) spectroscopy was performed using IRTF-TEXES (J. H. Lacy et al. 2002). In this paper, we focus on spectra recorded between 2019 April 16 and 2023 July 20 in settings centered at 587, 606, and 1248 cm^{-1}, which respectively capture the emission features of the hydrogen quadrupole (H_2 S(1)) line, the methyl radical (CH_3), and the *P*-branch of CH_4. Table A1 summarizes times, instrument configuration, and observing parameters of the IRTF-TEXES data presented in this paper. Although the observations recorded on 2019 April 16 and 2019 August 20 were previously presented in J. A. Sinclair et al. (2020), they are reanalyzed with improved methods in this paper (see Section 4.1 for further details).

2.1. Measurement Strategy

The slit of the instrument was aligned parallel to Jupiter's central meridian. Starting from dark sky off the western limb of the planet, the slit was stepped in increments of half a slit width over mid- to high northern latitudes, and a 4 s exposure was recorded at each step. The scan continued until several steps of dark sky east of the planet limb were recorded. The inclusion of planet-free dark sky at the beginning and end of the scan allows for efficient sky subtraction. A schematic of the scan is also shown in Figure 1 of J. A. Sinclair et al. (2018). A similar process was repeated at mid- to high southern latitudes. Northern and southern scans were then repeated in the remaining spectral settings. Scans over all spectral settings were repeated over the course of a night/over multiple nights in order to build up longitudinal coverage. A blackbody card mounted in the fore optics of the instrument served as both a flat-field and a radiometric standard. Further details on the observing strategy, reduction, and calibration are provided in J. A. Sinclair et al. (2018).

2.2. Spatial Coaddition

Spectra were sorted into 5°-wide latitude bins, Nyquist sampled by 2.°5. From 70°S to 50°N, all spectra were averaged into a single coadded spectrum that represents a longitudinal mean. At latitudes that include the northern auroral region (>55°N, planetocentric), spectra in a latitude circle were divided into two groups depending on whether they were at a longitude equatorward or poleward of the MAE (using the statistical mean position indicated in B. Bonfond et al. 2017) and coadded. These coadded spectra equatorward and poleward of the MAE are henceforth named the "non-auroral-mean" and "auroral-mean" spectra, respectively.

In order to compute a coadded spectrum of the southern auroral oval, we coadded spectra recorded between the 74°S latitude circle and the southern MAE: we exclude higher-latitude spectra in order to minimize the effects of diffraction blurring dark sky with signal from the planet. The regions adopted for spectral coaddition are further demonstrated in Figure 1. The noise on the coadded spectrum was assumed to be the larger of either the uncertainty on the mean ($\bar{\sigma} = (\sigma_1^2 + \sigma_2^2 + ... \sigma_N^2)^{1/2}/N$, where N is the number of individual spectra averaged) or the standard deviation on the mean.

We note that our spatial coaddition scheme averages over large areas where smaller-scale morphologies in the ultraviolet emissions are observed. For example, in Lyα emissions, discrete footprints of the satellites are observed equatorward of the MAE and smaller-scale, patchy/diffuse emissions are observed in the polar region (e.g., D. Grodent 2015, B. Bonfond et al. 2017). As far as we are aware, such morphologies have never been observed at mid-infrared wavelengths, because they are not resolved by the coarser spatial resolution achieved at such longer wavelengths and/or because the energy deposited does not reach the deeper altitudes sensed at mid-infrared wavelengths. In any case, such smaller-scale morphologies are not lost by our spatial coaddition scheme (since they are not observed in the first place). We opted for larger spatial ranges for coaddition in order to maximize the effective signal-to-noise ratio (SNR) in the coadded spectrum.

2.3. Radiometric Calibration Adjustment

In previous work, radiances in the 587 cm^{-1} spectra and 606 cm^{-1} spectra needed to be scaled by a factor of 1.3 and 1.4, respectively, such that the H_2 S(1), CH_3, and CH_4 features in the 587, 606, and 1248 cm^{-1} spectra, respectively, could be

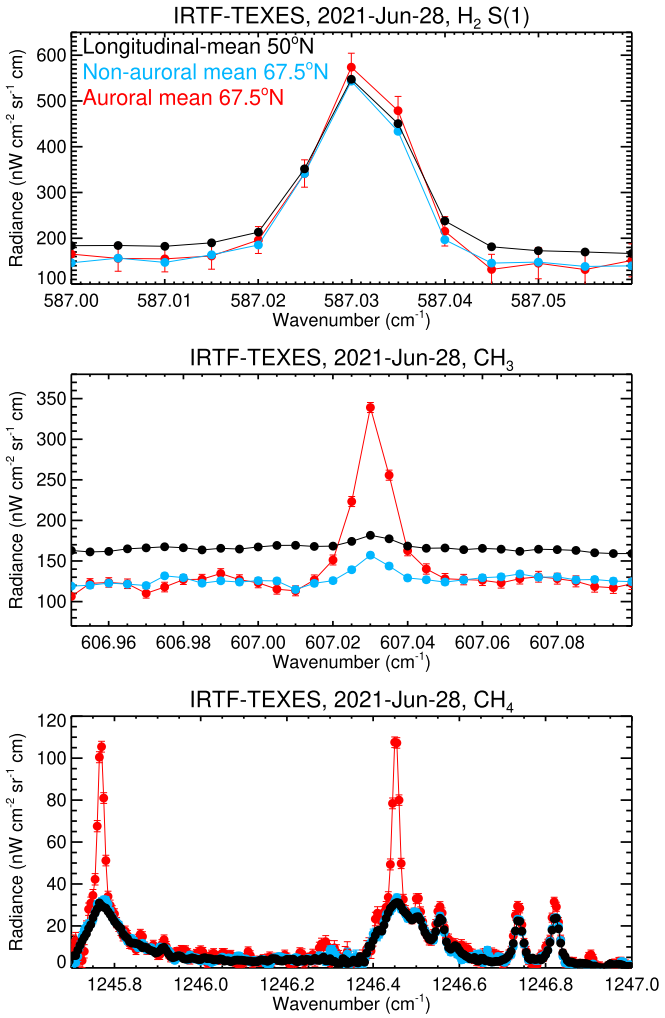

Figure 2. Spectra recorded by IRTF-TEXES on 2021 June 28 in the 587 cm^{-1}, (top panel), 606 cm^{-1} (middle panel), and 1248 cm^{-1} (bottom panel) spectral settings, which respectively capture emission features of the H_2 S(1) quadrupole line, CH_3, and CH_4. Black spectra are a longitudinal mean at 50°N, blue spectra are a nonauroral mean at 67.5°N, and red spectra are an auroral mean at 67.5°N (see Figure 1/Section 2 for further details on the spatial coaddition). Only a subset of the spectral ranges measured are shown for clarity.

simultaneously fit with the same temperature profile (J. A. Sinclair et al. 2018, 2020). This was attributed to some form of beam dilution in the longer-wavelength spectra. We tested simultaneous fitting of all three spectral settings/features on the newer observations presented in this work and found that the same scale factors were needed to optimize the spectral fits. We therefore perform the same adjustments to all 587 and 606 cm^{-1} IRTF-TEXES spectra presented in this work. Figure 2 shows examples of the coadded IRTF-TEXES spectra in all three spectral settings with the aforementioned corrections to the 587 and 606 cm^{-1} radiances.

3. SOFIA-EXES Observations

High-resolution (66,667 < R < 85,714) mid-infrared spectroscopy of Jupiter's mid- to high latitudes was performed using EXES (M. J. Richter et al. 2018) on SOFIA (P. Temi et al. 2018). A series of 2–3 hr observing runs were performed over successive nights from 2021 June 8 to 18. In this work, we present only measurements recorded in the 606 and 1299 cm^{-1} settings, which respectively capture the stratospheric emission features of the methyl radical, CH_3, and methane, CH_4. Observations were recorded at 634 cm^{-1} with the goal of capturing stratospheric emission from methylacetylene (CH_3C_2H): these measurements will be presented in future work. Observations were recorded while the aircraft cruised at ~43,000 feet and relative Earth–Jupiter velocities of <-24 km s^{-1}, which allowed Jovian CH_4 emission lines at ~1299 cm^{-1} to be recorded at high sensitivities with minimal obscuration by telluric CH_4. Table A2 summarizes times, instrument configuration, and observing parameters of the SOFIA-EXES data presented in this paper.

3.1. Measurement Strategy

The measurements were performed in a similar way to those for IRTF-TEXES (see Section 2), except the slit length was aligned parallel to the equator of Jupiter and scans were performed from midlatitudes toward each pole. The scans continued past each pole to include several exposures of dark sky for background subtraction and calibration. Scans were repeated over the course of the 2–3 hr available each night and on successive nights in order to build up longitudinal and temporal coverage. Observations recorded on 2021 June 10 and June 17 best sample the longitudes of the northern MAE (140°W–230°W, System III). A combination of observations recorded on 2021 June 10–11 and 17–18 sample the longitudes outside of or equatorward of the MAE with minimal time elapsed from those that sample the MAE. In this paper, we therefore present results using observations recorded on 2021 June 10–11 and 2021 June 17–18. Table A2 provides details on the SOFIA-EXES measurements analyzed in this work.

3.2. Spatial Coaddition

SOFIA's smaller primary aperture (2.5 m) and EXES's wider slit result in a lower effective spatial resolution on Jupiter compared to TEXES on the IRTF (3 m primary). We therefore omitted spectra recorded at latitudes poleward of ±70° (planetocentric), where diffraction is potentially mixing signal from the planet with the dark sky off the limb. As such, we cannot sufficiently constrain the CHA poleward of the southern MAE (<68°S). Individual spectra recorded on each night were similarly sorted in latitude–longitude ranges and coadded as for IRTF-TEXES observation (see Section 2, Figure 1) but using a coarser latitude grid of 8°-wide bins, Nyquist sampled by 4°.

3.2.1. Radiometric Calibration

We noticed that radiances in the 606 cm^{-1} setting were significantly lower than expected and compared to IRTF-TEXES observations. Figure 3 compares the continuum radiance at ~607 cm^{-1} using non-auroral-mean SOFIA-EXES observations recorded on 2021 June 10–11 and 17–18 with IRTF-TEXES observations recorded on 2021 June 28 (with the scale factor of 1.4 correction applied to the 606 cm^{-1} TEXES radiances, as detailed in Section 2.3). The continuum in the 606 cm^{-1} band is sensitive to temperature in the upper troposphere (~100 mbar), and no significant temporal variability in the zonal-mean temperature field would be expected over the period of 10–18 days between IRTF-TEXES and SOFIA-EXES measurements. We find that continua radiances in the SOFIA-EXES data are a factor of ~2 lower than those of IRTF-TEXES. The source of such a systematic offset is

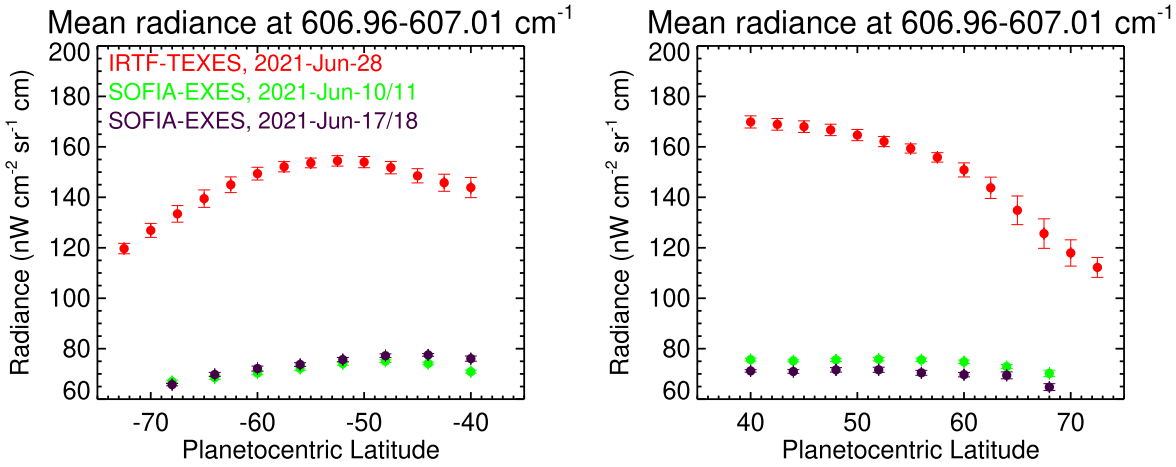

Figure 3. The longitudinal-mean radiance averaged between 606.96 and 607.01 cm^{-1}, which captures tropospheric continuum, using IRTF-TEXES measurements on 2021 June 28 (red) and SOFIA-EXES measurements on 2021 June 10/11 (green) and 2021 June 17/18 (dark purple). IRTF-TEXES results have been convolved in latitude such that they are at a similar spatial resolution to the SOFIA-EXES results.

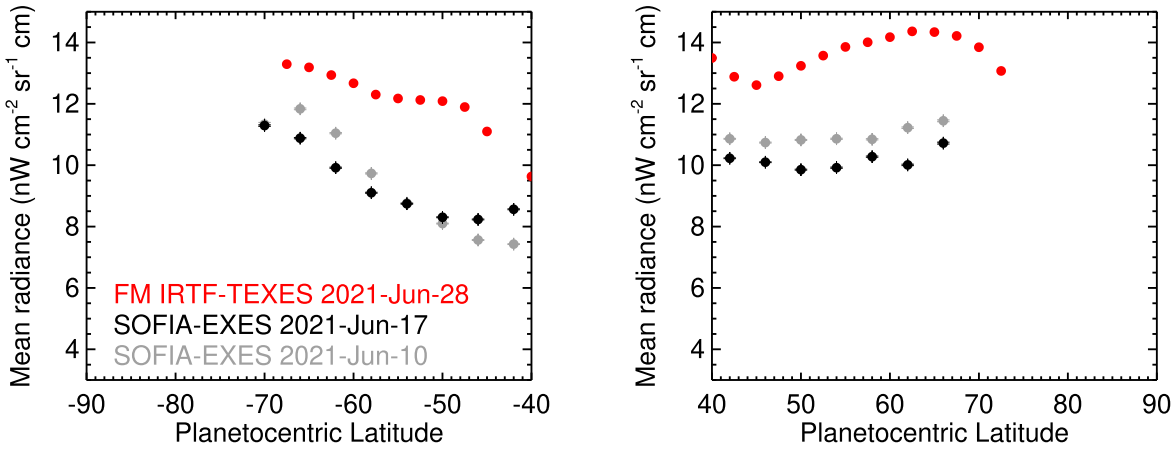

Figure 4. Mean radiances calculated over the ~1299 cm^{-1} bandpass for SOFIA-EXES observations recorded on 2021 June 10–11 (gray circles) and June 17–18 (black circles). Error bars on mean observed radiances are included but are too small to be seen on the range of the plot. Forward-modeled ("FM") radiances of IRTF-TEXES results derived from observations on 2021 June 28 are shown as red circles.

currently uncertain. The SOFIA-EXES observing run in 2021 June was affected by a deformed entrance window, which is a possible source of the discrepancy. In any case, a correction to the radiances in the 606 cm^{-1} spectral settings was needed to account for this. Experience indicates that the radiometric calibration of IRTF-TEXES data is robust from night to night (e.g., L. N. Fletcher et al. 2016), and thus we performed the correction by scaling the continua in the SOFIA-EXES 606 cm^{-1} data to match those of the IRTF-TEXES data.

We explored whether radiances in the 1299 cm^{-1} setting also needed to be corrected. IRTF-TEXES spectra were not recorded at 1299 cm^{-1}, and thus we could not test for an offset or perform a correction using the simple comparison of IRTF-TEXES and SOFIA-EXES radiances as above. Instead, using the methods described in Section 4, the meridional temperature distribution was retrieved from non-auroral-mean IRTF-TEXES observations recorded on 2021 June 28. The temperature distributions were then forward modeled over the wavenumber range and observing geometry of the 1299 cm^{-1} SOFIA-EXES observations recorded on 2021 June 10–11 and 17–18. For both the forward-modeled spectra and the observed spectra, a mean radiance across the 1299 cm^{-1} setting, which includes both continuum and emission lines of CH_4, was calculated as a function of latitude, as shown in Figure 4. We find that SOFIA-EXES radiances are a factor of ~1.4 lower than a forward model of IRTF-TEXES results on 2021 June 28. As noted above, we would expect insignificant temporal variability in the zonal-mean temperature profile outside of the auroral region over a timescale of 10–18 days. We therefore attribute the offset of a factor of 1.4 between SOFIA-EXES and IRTF-TEXES radiances to also result from an uncertainty in the radiometric calibration. In the remainder of the paper, spectra and results derived from SOFIA-EXES measurements use scale factors of 2.0 and 1.4 applied to the 606 and 1299 cm^{-1} spectral settings, respectively. Figure 5 shows examples of observed SOFIA-EXES spectra with the aforementioned scale factors applied.

4. Analysis

4.1. Radiative Transfer Model

The NEMESIS radiative transfer model (P. G. J. Irwin et al. 2008) was adopted for all forward modeling and retrievals of atmospheric information. NEMESIS adopts the optimal estimation technique in constraining atmospheric information, where an initial guess or a priori value/profile of each variable parameter (e.g., temperature) is assumed, a forward model is computed and compared with the observation, and the free

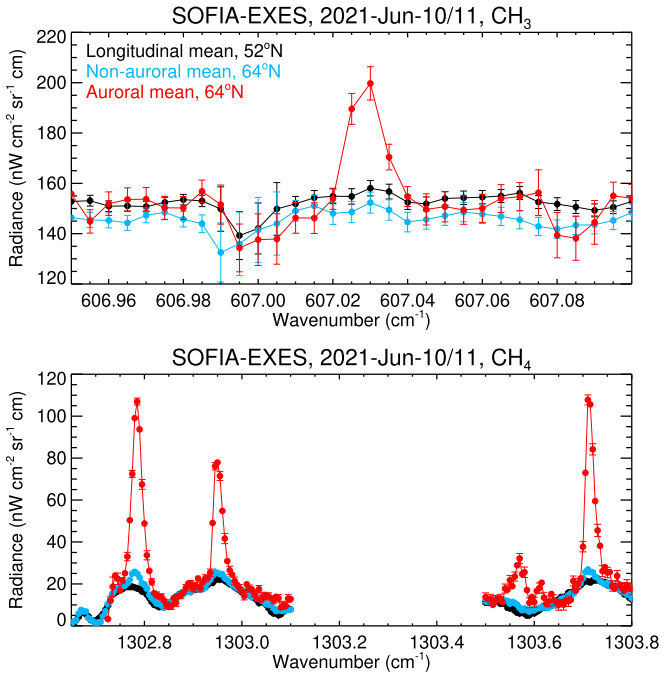

Figure 5. Spectra recorded by SOFIA-EXES on 2021 June 10–11 in the 606 cm^{-1} (top panel) and 1248 cm^{-1} (bottom panel) spectral settings, which respectively capture emission features of CH_3 and CH_4. Black spectra are a longitudinal mean at 52°N, blue spectra are a nonauroral mean at 64°N, and red spectra are an auroral mean at 64°N (see Figure 1/Section 2 for further details on the spatial coaddition). Only a subset of the spectral ranges measured are shown for clarity.

parameter is adjusted iteratively until the quality of fit of the forward model to the observation is optimized. Further details on the NEMESIS code can be found in P. G. J. Irwin et al. (2008).

The correlated-*k* treatment (e.g., A. A. Lacis & V. Oinas 1991) of spectroscopic line data was adopted for computational efficiency. J. A. Sinclair et al. (2020, and references therein) provide details on the sources of spectroscopic line data for H_2, NH_3, PH_3, CH_4 and its isotopologues, and photochemical by-products. For IRTF-TEXES, *k*-distributions were computed at the spectral resolving powers in each setting, assuming a sinc-squared function, and subsequently concatenated such that spectra in all three settings could be modeled/inverted simultaneously. Similarly, *k*-distributions were computed at the spectral resolving powers achieved by SOFIA-EXES in the 606 and 1299 cm^{-1} spectral settings and subsequently concatenated.

4.2. Atmospheric Model

The vertical profiles of CH_4, and its photochemical by-products, were adopted from a grid of photochemical models. The photochemical model is based on that presented in J. I. Moses & A. R. Poppe (2017) but outputted at a latitude of 60°N and computed over a range of eddy diffusion coefficient profiles to produce a range of CH_4 homopause pressures. The model assumed influx rates of 4×10^4 cm^{-2} s^{-1}, 7×10^6 cm^{-2} s^{-1}, and 1×10^5 cm^{-2} s^{-1} for H_2O, CO, and CO_2, respectively, in order to match abundances of these species derived in E. Lellouch et al. (2002, 2006) and B. Bézard et al. (2002). However, we would expect the neutral hydrocarbon species to exhibit negligible dependence on the assumed influx rates of H_2O, CO, and CO_2.

The models are numbered in order of highest to lowest homopause pressure and include a "b" suffix to distinguish them from a similar but smaller grid of models presented in J. A. Sinclair et al. (2020). The same model grid was also adopted in a recent analysis of mid-infrared observations recorded by the James Webb Space Telescope (JWST), though with a different naming scheme (P. Rodrìguez-Ovalle et al. 2024): "Mod. 0" and "Mod. 12" in their work are identical to Models 1b and 13b presented in this paper. We retain the 1b, 2b, ..., 13b naming scheme in this paper for ease of comparison with the similar but smaller model grid presented in J. A. Sinclair et al. (2020).

Figure 6 summarizes the pressure levels and eddy diffusion coefficients at the homopause for each model and the corresponding vertical profiles of CH_4 and CH_3. For the vertical temperature profile, we assumed the profile adopted in J. I. Moses & A. R. Poppe (2017, and references therein). The vertical profiles of H_2, He, NH_3, and PH_3 were adopted from J. A. Sinclair et al. (2020) and are fixed for Models 1b to 13b.

4.3. Vertical Sensitivity

The vertical contribution functions were calculated at 606 and 1245 cm^{-1} for IRTF-TEXES and at 606 and 1299 cm^{-1} for SOFIA-EXES. The vertical contribution functions, dR/dT_i, where R is the radiance and T_i is temperature at the ith atmospheric level, describe the relative contribution of each atmospheric level to the total radiance observed at the top of the atmosphere.

Model 7b (Figure 6) was adopted as the atmospheric model for calculations of the vertical contribution functions, since we found that this model generally provided the best fits to the auroral-mean observations (see Section 2.2). Calculations were performed at an emission angle of 60° to capture the viewing geometry of observing mid- to high latitudes. For IRTF-TEXES, the 2D (wavenumber–pressure) contribution function image was Doppler shifted by −22 km s^{-1}, which is the smallest Doppler shift of the TEXES observations presented in this work (Table A1), to simulate the relative Earth/Jupiter velocity when observing. The resulting image was then convolved with the telluric transmission function assuming the 4205 m (~13,800-ft) altitude of Maunakea, a precipitable water vapor (PWV) of 1 mm, and a zenith angle of 45°. Similarly, the contribution functions calculated for SOFIA-EXES were Doppler shifted by −24 km s^{-1}, which is the smallest relative Earth–Jupiter velocity of the SOFIA-EXES observations presented in this work (Table A2), and then convolved with telluric transmission spectra assuming an altitude of 12,480 m, a PWV of 0.5 mm, and a zenith angle of 45°.

Figures 7(a)–(d) shows the resulting two-dimensional images of the vertical contribution functions, and Figure 7(e) shows the mean contribution function calculated across the observed spectral range. For both IRTF-TEXES and SOFIA-EXES, the 606 cm^{-1} spectral setting captures tropospheric continuum, which peaks in contribution at ~100 mbar, and the emission feature of CH_3 at 607.03 cm^{-1}, which sounds the atmosphere at approximately microbar pressures.

For IRTF-TEXES, observations of CH_4 target the *P*-branch of the ν_4 band at ~1248 cm^{-1}. The *P*-branch is chosen as a compromise between measuring a sufficient number of Jovian CH_4 emission lines and minimizing the obscuration by telluric CH_4 and therefore not requiring unreasonably long exposure times for a sufficient SNR. Over the ~8 cm^{-1} bandpass, a mixture of stronger and weaker CH_4 emission lines are captured, which collectively sound the atmosphere from

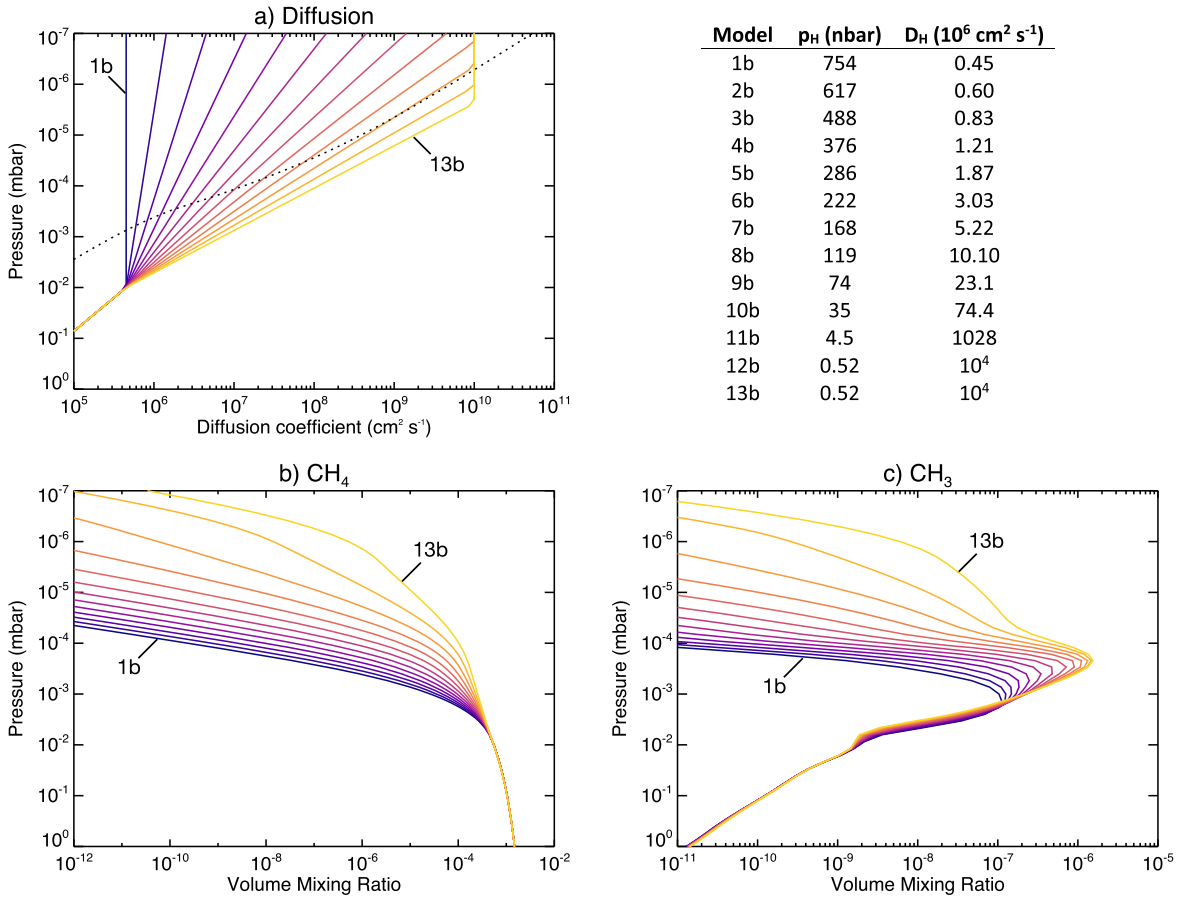

Model	p_H (nbar)	D_H (10^6 cm^2 s^{-1})
1b	754	0.45
2b	617	0.60
3b	488	0.83
4b	376	1.21
5b	286	1.87
6b	222	3.03
7b	168	5.22
8b	119	10.10
9b	74	23.1
10b	35	74.4
11b	4.5	1028
12b	0.52	10^4
13b	0.52	10^4

Figure 6. The family of photochemical models adopted in this work. Panel (a) shows the vertical profiles of the eddy diffusion coefficient (solid, colored lines) and the molecular diffusion coefficient profile (black, dotted). Panels (b) and (c) show the corresponding vertical profiles of CH_4 and CH_3, respectively. The homopause pressure levels and the eddy diffusion coefficient at the homopause of each model are shown in the legend.

~50 mbar to ~0.5 μbar. Inversions of the IRTF-TEXES observations also include the H_2 S(1) quadrupole feature at 587.03 cm^{-1}, which sounds the atmosphere from 200 to 50 mbar (see Figure 4 of J. A. Sinclair et al. 2020). Thus, inversion of the IRTF-TEXES observations allows the vertical temperature profile to be retrieved from ~200 mbar to 0.5 μbar.

SOFIA-EXES observations are performed at higher altitudes in Earth's atmosphere, above a larger majority of telluric CH_4, and thus the Q-branch (~1305 cm^{-1}) of the ν_4 band can be measured with a sufficient SNR in reasonable exposure times. In targeting the Q-branch and achieving a large bandpass (~10 cm^{-1} compared to TEXES), SOFIA-EXES can measure a larger number of stronger CH_4 lines in a single observation (see Figure 7(d)), which in turn extends the vertical sensitivity to higher altitudes. This is also demonstrated in Figure 7(e), which shows the mean contribution function calculated over each bandpass.

4.4. Constraining the CH_4 Homopause Level

In order to constrain the level of the CH_4 homopause, we performed a similar approach to that detailed in J. A. Sinclair et al. (2020). Initially, Model 1b (Section 4.2) was adopted as the atmospheric model, and the vertical profiles of all gases, including CH_4 and CH_3, were fixed. For all longitudinal-mean and non-auroral-mean SOFIA-EXES spectra (see Sections 3), the emission features of CH_3 and CH_4 were inverted simultaneously, and (only) the vertical temperature profile was allowed to vary. For the auroral-mean spectra, we found that we needed to vary both the vertical profile of temperature and CH_3 in order to fit the emission feature of CH_3 within uncertainty. We attribute the need to vary CH_3 in order to fit spectra poleward of the MAE to result from uncertainties in the CH_3 chemical kinetics (e.g., M. Dobrijevic et al. 2003; 2010).

The absolute χ^2 (Equation (1)) was calculated in order to quantify the quality of fit to the spectra:

$$\chi^2 = \sum_i^N \left(\frac{O_i - M_i}{\sigma_i} \right)^2. \quad (1)$$

O_i, M_i, and σ_i are respectively the observed radiance, modeled radiance, and uncertainty on radiance at the ith spectral point, and N is the number of spectral points. This process was then repeated adopting Models 2b to 13b in turn, thereby producing an absolute χ^2 versus homopause pressure curve (e.g., Figure 8) for each location. The homopause pressure that minimized χ^2 was assumed to be the homopause level for that location. Lower and upper 1σ confidence levels (uncertainties) were determined by interpolation of the χ^2 versus logarithmic homopause pressure curve to the points where $\chi^2 = \chi^2_{\min} + 1$ (W. H. Press et al. 1992). For each model, the retrieved temperature–pressure profile was used to convert the homopause pressure (Figure 6) into an altitude with respect to the 1 bar level. This produced an absolute χ^2 versus homopause altitude curve, from which the best-fitting homopause altitude and lower and upper confidence intervals were also determined.

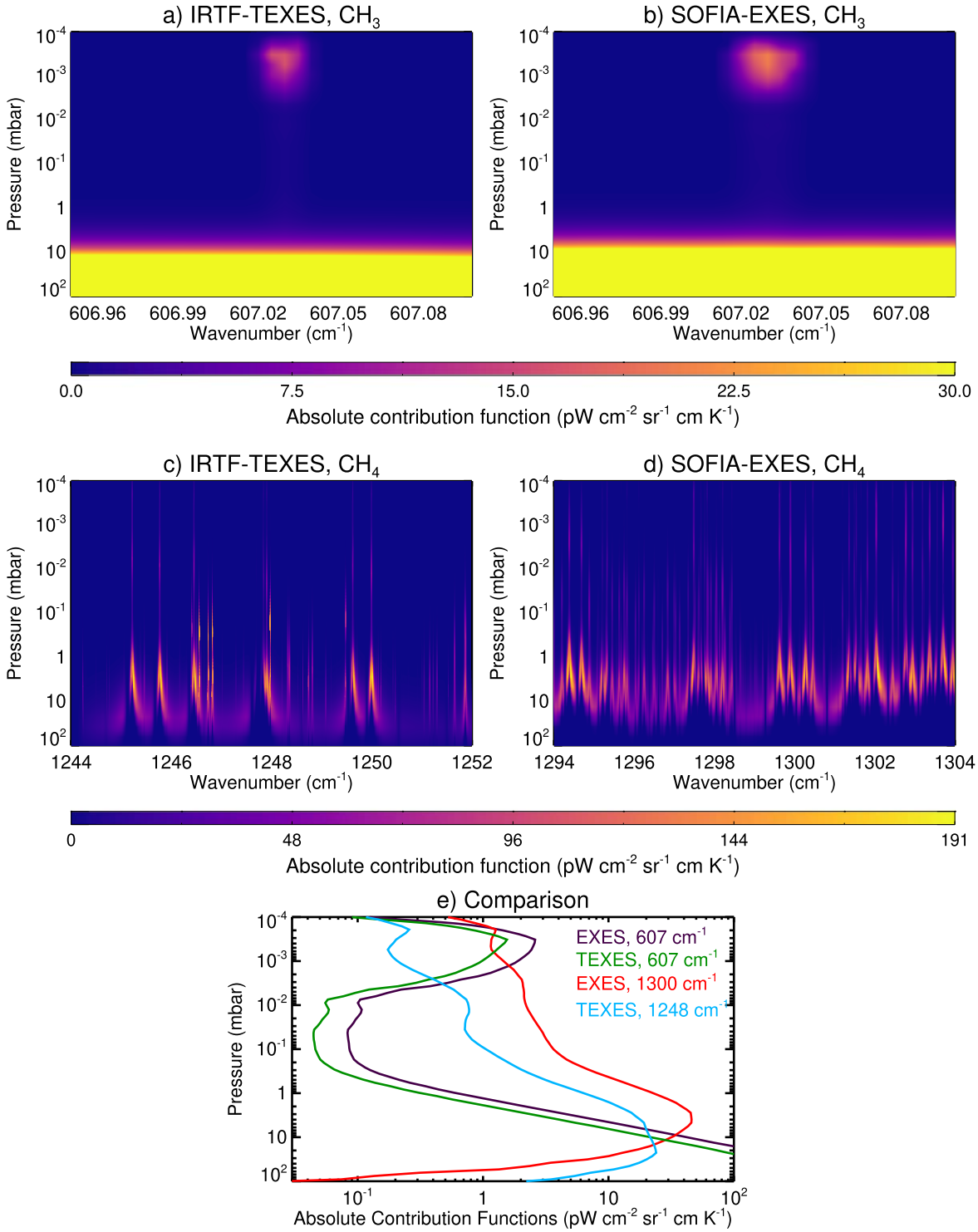

Figure 7. The vertical contribution functions of the spectral settings/instruments analyzed in this work, which describe the relative contribution of each atmospheric level to the total radiance observed at the top of the atmosphere. Panels (a) and (b) show the contribution functions over a subset of the 606 cm^{-1} spectral setting, which captures CH_3 emission, for IRTF-TEXES and SOFIA-EXES, respectively. Panels (c) and (d) show the contribution functions of IRTF-TEXES at 1248 cm^{-1} and SOFIA-EXES at 1299 cm^{-1}, respectively. Panel (e) compares the mean contribution function for each spectral setting/instrument.

This is exemplified in Figure 8 for SOFIA-EXES observations recorded at 60°N on 2021 June 10–11. Using a mean of all spectra recorded poleward of the MAE, Model 9b yields the best quality of fit to the observations with a CH_4 homopause location of $\log(p_H\ (\text{nbar})) = 1.86^{+0.51}_{-0.48}$ in pressure space and $z_H = 402^{+79}_{-57}$ km above 1 bar in altitude space. In contrast, using a mean of all spectra recorded equatorward of the MAE, we find that Model 1b, the lowest-altitude homopause model, yields the best fit. There is no parameter space toward lower homopause altitudes/higher homopause pressures to determine whether Model 1b is truly the best-fitting model or to determine a lower confidence level in altitude space or an upper confidence level in pressure space. We

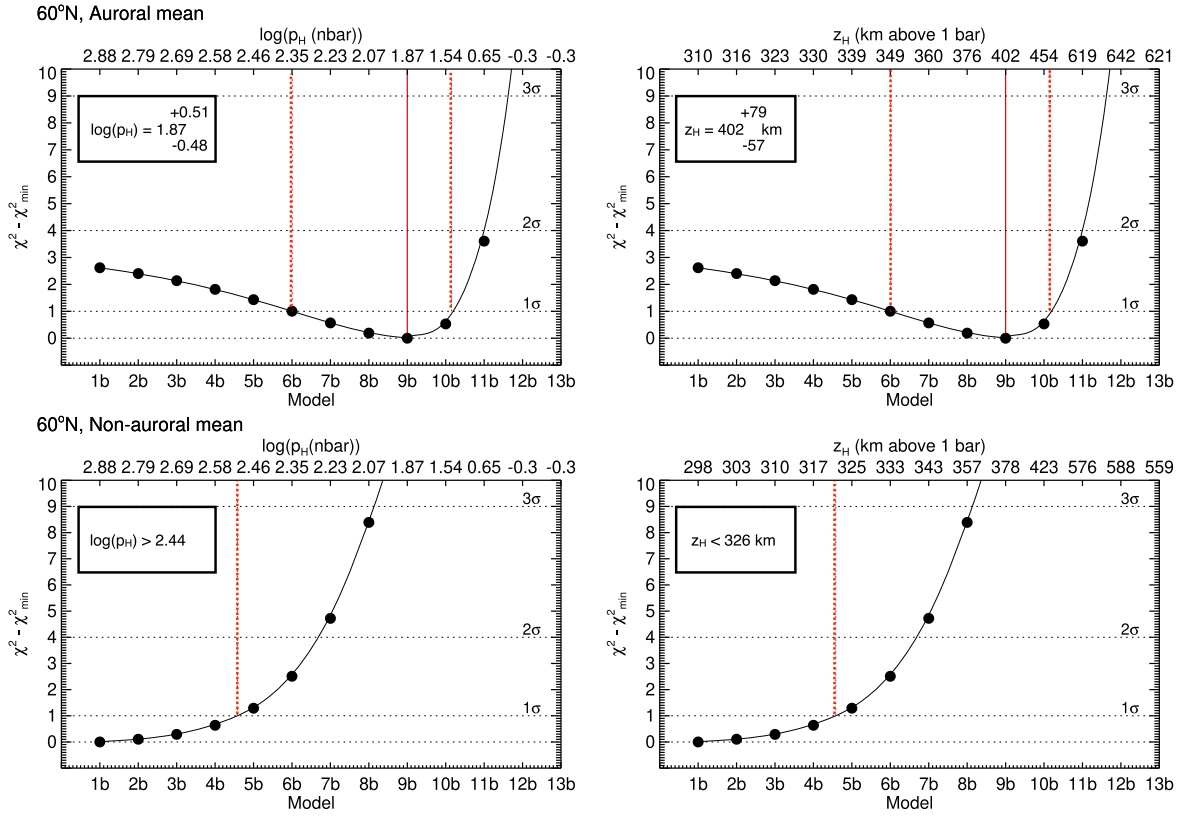

Figure 8. Variations in the χ^2 (Equation (1)) as a function of the model tested in inverting SOFIA-EXES spectra recorded on 2021 June 10–11. The top and bottom panels show the results at 60°N using the auroral-mean spectra and non-auroral-mean spectra, respectively. In the left column, the upper *x*-axis shows the variation in χ^2 with respect to homopause altitude; in the right column, the upper *x*-axis shows the variation with respect to homopause pressure. Vertical solid and dotted red lines indicate the best-fitting homopause location and 1σ confidence levels, respectively.

therefore quote the upper 1σ confidence interval of 326 km above 1 bar as the upper limit in altitude space and a lower limit of $\log(p_H) > 2.44$ in pressure space.

For IRTF-TEXES observations, a very similar retrieval process to that for the SOFIA-EXES data was adopted, but with exception that the H_2 S(1) quadrupole feature at 587.03 cm^{-1} was included. This feature constrains the lower-stratospheric temperature profile (e.g., J. A. Sinclair et al. 2018, 2020) and was therefore included for the sake of completeness. Ultimately, we found that the inclusion or omission of the H_2 S(1) feature had negligible effect on the temperature profile retrieved from IRTF-TEXES data, as evidenced by the test case presented in Appendix D. For this reason, we consider the SOFIA-EXES and IRTF-TEXES results to be directly comparable, even if the H2 S(1) feature was not available in the former data set. We present the IRTF-TEXES results as is rather than repeating the analysis without the H_2 S(1) feature.

The uncertainties on the homopause level in the direction of the top of the atmosphere (i.e., the upper uncertainty in altitude or the lower uncertainty in pressure) are significant, particularly for IRTF-TEXES results poleward of the MAE. This prevents latitudinal variations in the CH_4 homopause level within or poleward of the MAE from being assessed. We also tested dividing spectra poleward of the MAE into sectors resolved in longitude and found that the large error bar in CH_4 homopause level toward the top of the atmosphere prevented longitudinal variations poleward of the MAE from being assessed. The large uncertainty on derived CH_4 homopause levels toward the top of the atmosphere does not result from a limited vertical sensitivity but instead results predominantly from the limited vertical sensitivity of the observations to pressures lower than 0.1 μbar (Figure 7). This is therefore an issue that is not resolved by coadding a greater number of spectra together in order to reduce the effective noise. Nevertheless, we can robustly constrain the CH_4 homopause level equatorward of the MAE (since it is generally at higher pressures/lower altitudes, where there is greater sensitivity in the observations) and derive a robust lower limit in altitude or upper limit in pressure of the CH_4 homopause level poleward of the MAE.

5. Results

5.1. Northern Hemisphere Results

Figures 9 and 10 show the derived locations of the CH_4 homopause at mid- to high northern latitudes in both pressure and altitude space, using IRTF-TEXES and SOFIA-EXES observations recorded between 2019 April 16 and 2023 July 20. In order to test whether the regions poleward of the northern MAE are subject to enhanced vertical transport compared to elsewhere on the planet, we compare derived homopause levels poleward of the northern MAE with the region equatorward but in the same latitude circle. In performing this comparison, we find that results can be split into three categories.

First, for a subset of latitudes/times, we find that derived locations of the homopause poleward and equatorward of the MAE in the same latitude circle agree within uncertainty in both pressure and altitude space. For example, using the non-auroral-mean result at 65°N derived from IRTF-TEXES observations on 2021 November 8, we find a CH_4 homopause location of $\log(p_H(\text{nbar})) = 2.23^{+0.39}_{-0.21}$ or $z_H = 344^{+22}_{-31}$ km above 1 bar. Using

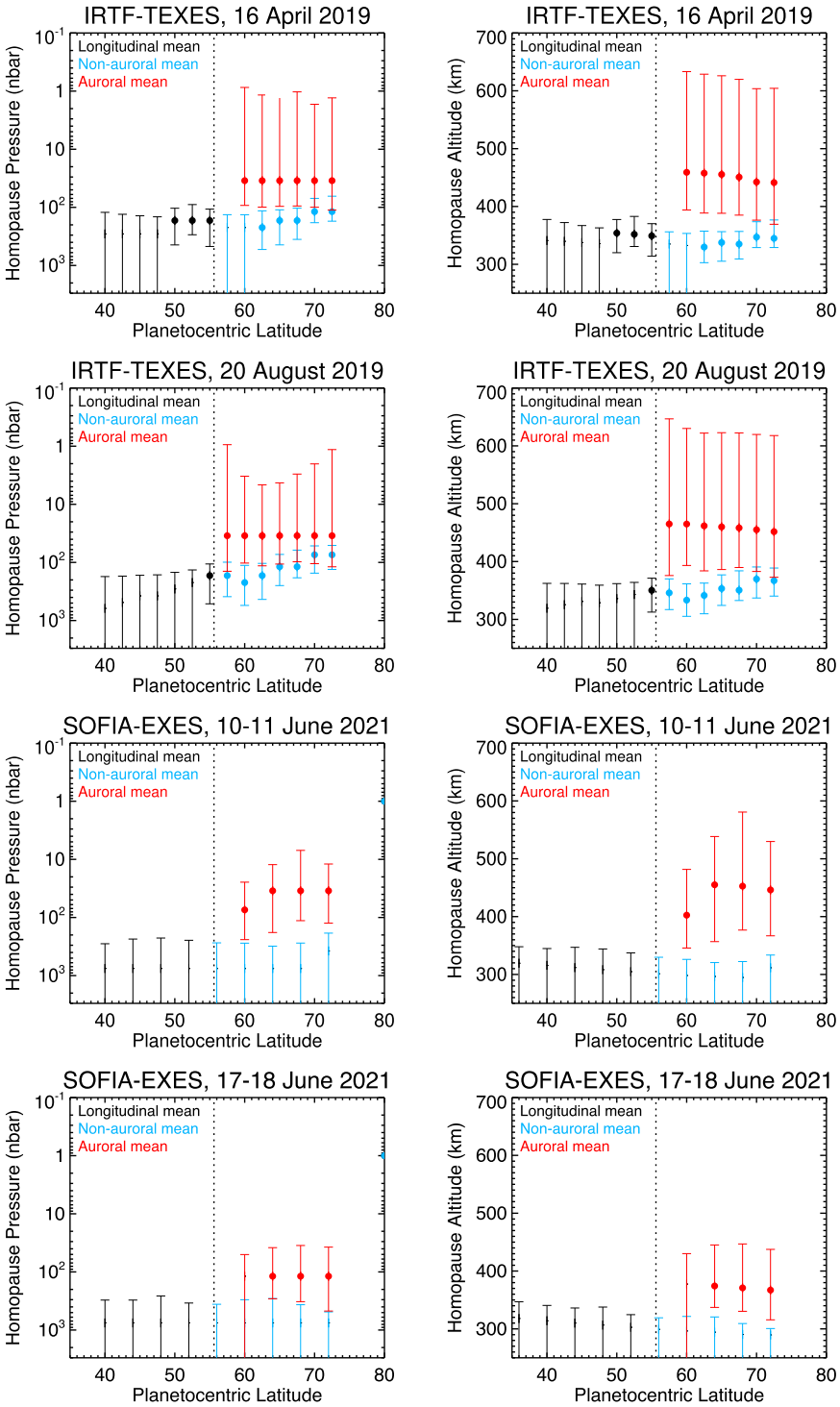

Figure 9. The location of the CH_4 homopause as a function of latitude at mid- to high northern latitudes, as derived from IRTF-TEXES observations on 2019 April 16 (top row) and 2019 August 20 (second row) and SOFIA-EXES observations on 2021 June 10–11 (third row) and 2021 June 17–18 (fourth row). Results are shown in both pressure space (left column) and altitude space (right column). Black results denote a longitudinal mean, blue results denote the nonauroral mean, and red results denote an auroral mean using—see Figure 1 for further details. Results where only an upper error bar in altitude or a lower error bar in pressure is shown indicate that only an upper or lower limit could be derived. Vertical dashed lines mark the lowest-latitude extent of the northern MAE (B. Bonfond et al. 2017).

instead the auroral-mean result at the same latitude on the same date, we derive a CH_4 homopause location of $\log(p_H) = 1.87^{+0.32}_{-0.53}$ or $z_H = 395^{+84}_{-37}$ km above 1 bar. In fact, for all latitudes north of ~55°N on 2021 November 8, derived CH_4 locations poleward and equatorward of the MAE are in agreement within uncertainty in both pressure and altitude space.

Second, for a subset of locations/times, in comparing results poleward and equatorward of the MAE, there is marginal or negligible difference in the CH_4 location in pressure space but a statistically significant difference in altitude space. For example, using IRTF-TEXES observations recorded on 2019 August 20, the derived CH_4 homopause location equatorward

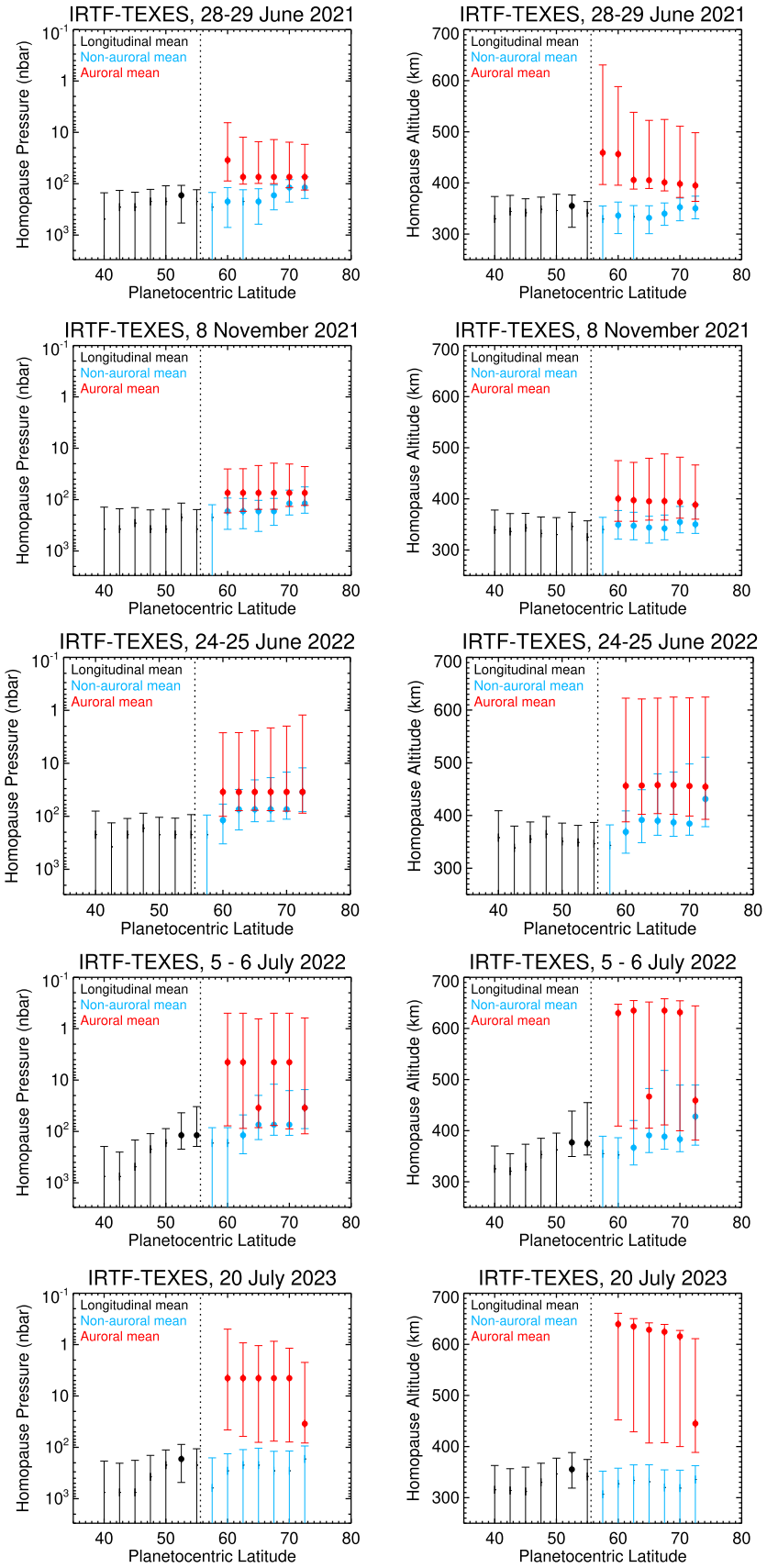

Figure 10. Same as Figure 9, but using IRTF-TEXES observations recorded on 2021 June 28–29 (top row), 2021 November 8 (second row), 2022 June 24–25 (third row), 2022 5–6 July (fourth row), and 2023 July 20 (fifth row).

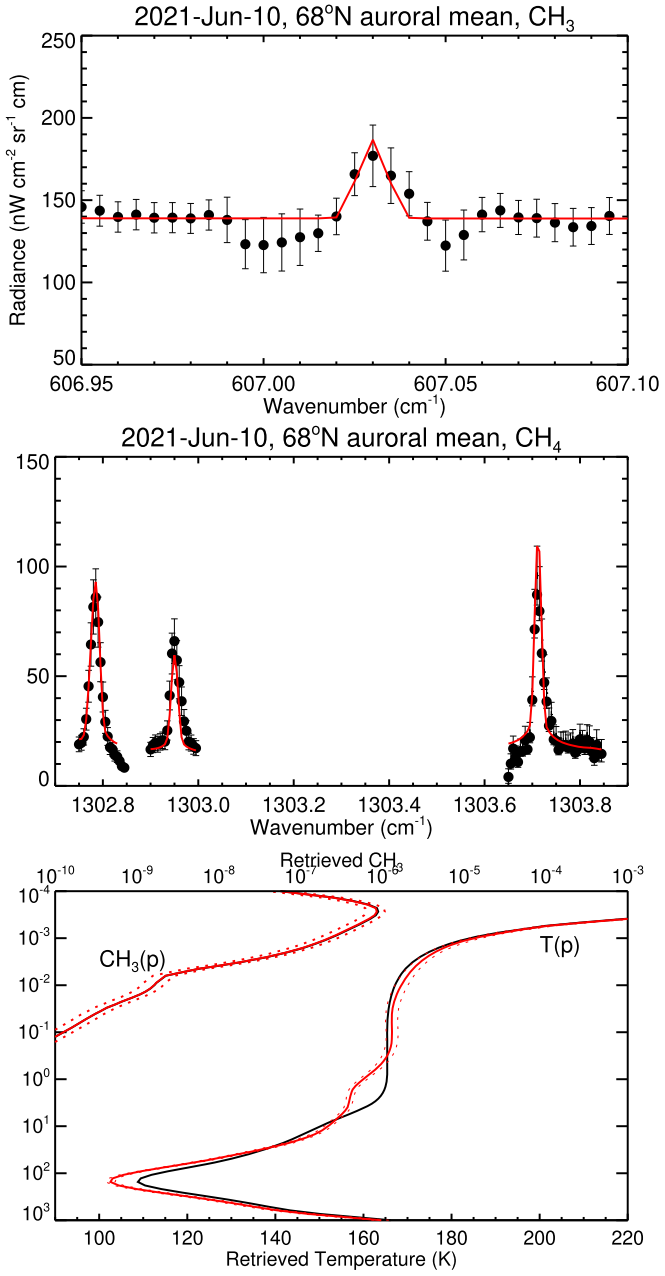

Figure 11. Observed SOFIA-EXES auroral-mean spectra (points with error bars) at 68°N of the CH_3 (top panel) and CH_4 (middle panel) emission on 2021 June 10. The best-fitting model spectrum is included as the solid red line. The bottom panel shows the corresponding retrieved profiles (solid red lines) and uncertainty (dotted red lines) of temperature (according to the lower *x*-axis) and CH_3 volume mixing ratio (according to the upper *x*-axis). The vertical profile of CH_3 is from Model 10b, which is the best-fitting model at this latitude/date.

of the MAE at 62.5°N is $\log(p_H) = 2.23^{+0.32}_{-0.20}$ and $z_H = 342^{+22}_{-26}$ km above 1 bar, and poleward of the MAE, $\log(p_H) = 1.54^{+0.51}_{-0.70}$ and $z_H = 453^{+128}_{-76}$ km.

Third, in the remaining results, there is a statistically significant difference in the CH_4 homopause level in both pressure and altitude space in comparing results between equatorward and poleward regions. For example, using SOFIA-EXES observations recorded on 2021 June 10, at 68°N, poleward of the MAE, we derive a homopause level of $\log(p_H) = 1.54^{+0.51}_{-0.69}$ and $z_H = 453^{+128}_{-76}$ km, compared to a lower limit of $\log(p_H) > 2.43$ and upper limit of $z_H < 322$ km derived equatorward of the MAE. Figure 11 shows the observed SOFIA-EXES auroral-mean spectra at 68°N, the best-fitting synthetic spectra, and the corresponding retrieved profiles of temperature and CH_3.

We note that upper confidence levels on the homopause location are smaller (by a factor of ~1.5) when derived from SOFIA-EXES observations compared to IRTF-TEXES observations. This demonstrates the benefit of observing with SOFIA-EXES, which can measure the *Q*-branch CH_4 emission at ~1299 cm^{-1}. EXES's bandpass at 1299 cm^{-1} samples a greater number of strong emission lines of CH_4, which extends the vertical range of sensitivity to higher altitudes/lower pressures (see Figure 7). At lower altitudes in Earth's atmosphere, IRTF-TEXES instead targets the *P*-branch of the CH_4 emission at ~1245 cm^{-1} to avoid unreasonably longer exposure times. This results in less sensitivity to higher altitudes as described further in Section 4.3.

Our results also allow the temporal variability of the thermal structure at high northern latitudes to be determined. Figure 12 shows retrieved temperatures at 60°N–62.5°N both poleward and equatorward of the MAE as a function of time and altitude. In the lower stratosphere, and equatorward of the MAE, we find that there is an overall ~5–10 K warming trend in comparing retrieved temperatures from 2019 April to 2023 July. This is expected given the increasing solar insolation at Jupiter's high northern latitudes over this time period, with the northern spring equinox ($L_s = 0°$) occurring in 2021 May. Poleward of the MAE, retrieved temperature profiles do not exhibit an overall long-term trend but instead vary erratically with ~5–10 K variability in time at ~1 mbar and ~20 K variability at 0.01 mbar. This is expected given that this region of the atmosphere is modulated by forcing from the magnetosphere and solar wind environment on timescales of several days. On a given date, the spread of temperatures at different pressure levels indicates the shape of the vertical temperature profile. For a subset of dates (i.e., 2021 June 28, 2022 June 24, 2022 July 6, 2023 July 20), temperatures retrieved poleward of the northern MAE are warmer at 2 mbar compared to 0.3 mbar, demonstrating the presence of auroral-related heating at ~1 mbar and relatively less heating at ~0.1 mbar, as noted in previous work (e.g., J. A. Sinclair et al. 2017b, 2017a, 2019). We also note that for the temperature profiles retrieved poleward of the northern MAE on 2021 November 8, 2022 June 24, and 2023 July 20, temperatures from 2 mbar to 0.01 mbar agree within uncertainty, indicating relatively isothermal temperature profiles over this pressure range. We discuss our interpretation of this result in Section 6.

The results in Figure 12 also indicate that there is no significant variability in the abundance of CH_3 at 0.001 mbar (with respect to uncertainty). However, we cannot rule out variability of ~0.1 ppmv, which is the approximate size of uncertainties on retrieved CH_3 abundances.

5.2. Southern Hemisphere Results

Observations recorded on 2021 June 29, 2021 November 8, 2022 June 25, 2022 July 6, and 2023 July 20 sufficiently sample longitudes poleward of the southern MAE. Figure 13 shows derived levels of the CH_4 homopause as a function of mid- to high southern latitudes. We find that for all dates where the region poleward of the southern MAE was sampled, derived homopause levels are in agreement within uncertainty with those derived equatorward of the MAE at 65°S. For

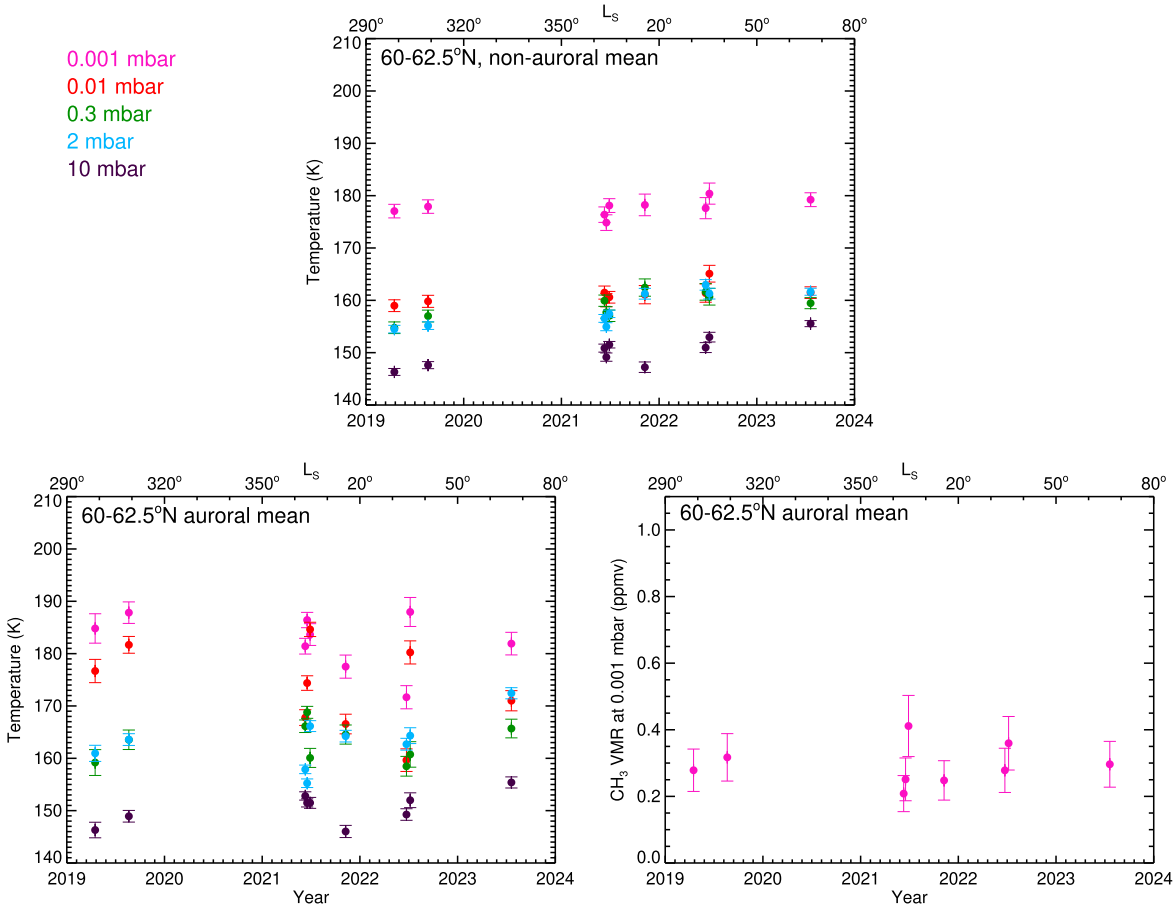

Figure 12. Top panel: retrieved temperature profiles (solid colored lines) and uncertainty (dotted colored lines) using the non-auroral-mean spectra at 62.5°N for IRTF-TEXES results and 60°N for SOFIA-EXES results. Results are colored according to the pressure level, as indicated by the legend on the left. The bottom left panel shows similar results for temperatures retrieved from auroral-mean spectra (poleward of the MAE) at 60°N–62.5°N. The bottom right panel shows retrieved profiles of CH_3, which was allowed to vary in fitting the auroral-mean spectra. Only the 1 μbar results are shown where there is sensitivity to CH_3 (see Figure 7).

example, using IRTF-TEXES observations recorded on 2021 June 28, we derive a CH_4 homopause level of $\log(p_H) = 1.87^{+0.31}_{-1.03}$ or $z_H = 396^{+171}_{-437}$ km poleward of the southern MAE. The observed spectra and the retrieved profiles of temperature, CH_3, and synthetic spectra associated with the best-fitting model are shown in Figure 14. At 65°S, we derive a lower limit of $\log(p_H) > 2.28$ and an upper limit of $z_H > 336$ km. Thus, either the region poleward of the southern MAE (at least the small segment that can be sampled from Earth) does not appear to be subject to enhanced vertical transport compared to the atmosphere equatorward of the southern MAE, or any difference in vertical transport is smaller than uncertainty. We also note that from the limited spatial resolution of NASA's IRTF and the highly foreshortened viewing of the southern auroral region from Earth, we can only sample the very edge of the region poleward of the MAE. It is possible that the level of the CH_4 homopause is enhanced significantly in regions further poleward of the MAE that are not resolved from 3 m Earth-based telescopes.

Figure 15 shows retrieved temperatures using a zonal mean of observations at 65°S (equatorward of the southern MAE) and retrieved temperatures and CH_3 abundances poleward of the southern MAE as a function of time. At 65°S, there is variability of <4 K at pressures higher than 0.01 mbar. On a given date, generally temperatures at 10 mbar are 5–10 K cooler than those at 2 mbar, temperatures from 2 to 0.01 mbar overlap within uncertainty, and 0.001 mbar temperatures are 15–20 K warmer than those at 0.01 mbar. This indicates a pronounced stratopause at ~1 mbar and a near-isothermal profile in temperature between 1 and 0.01 mbar, before reaching the base of the thermosphere, where temperatures rapidly increase with height. Poleward of the southern MAE, there is <4 K variability in temperature at the 1 mbar level, increasing to ~20 K variability at pressures lower than 0.1 mbar, with variability likely driven by magnetospheric forcing and/or solar wind variations. CH_3 abundances also exhibit variability by a factor of ~4. We discuss this variability further in Section 6.

6. Discussion

6.1. Spatial/Temporal Variability of the Homopause Level

6.1.1. Northern Auroral Region

Our analysis of IRTF-TEXES and SOFIA-EXES observations of Jupiter's mid- to high latitudes recorded between 2019 April and 2023 July allows us to derive the location of the CH_4 homopause as a function of location at mid- to high northern latitudes. Details on the observations are provided in Sections 2 and 3 and listed in Tables A1 and A2.

Figures 9, 10, and 13 show meridional and longitudinal variations of derived homopause levels at mid- to high latitudes in both hemispheres. In order to test whether the regions poleward of the northern MAE are subject to enhanced vertical transport compared to elsewhere on the planet, we compare derived

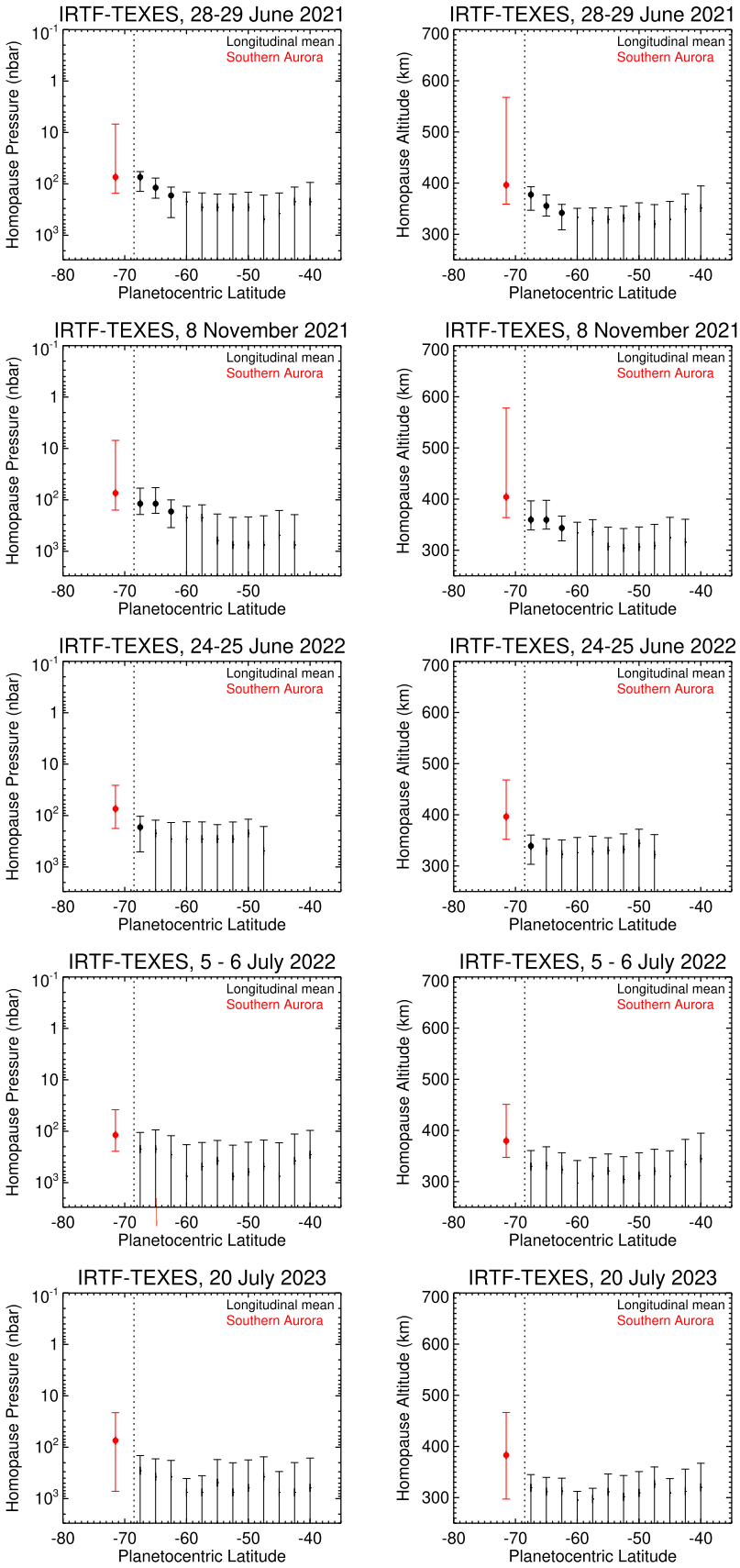

Figure 13. The location of the CH_4 homopause as a function of latitude at mid- to high southern latitudes, as derived from IRTF-TEXES observations on 2021 June 28–29 (top row), 2021 November 8 (second row), 2022 June 24–25 (third row), 2022 July 5–6 (fourth row), and 2023 July 20 (fifth row). Results are shown in both pressure space (left column) and altitude space (right column). Black results denote a longitudinal mean where all sampled longitudes were coadded into a single spectrum. Red results sample longitudes poleward of the southern MAE. Results where only an upper error bar in altitude or a lower error bar in pressure is shown indicate that only an upper or lower limit could be derived. Vertical dashed lines mark the lowest-latitude extent of the southern MAE (B. Bonfond et al. 2017).

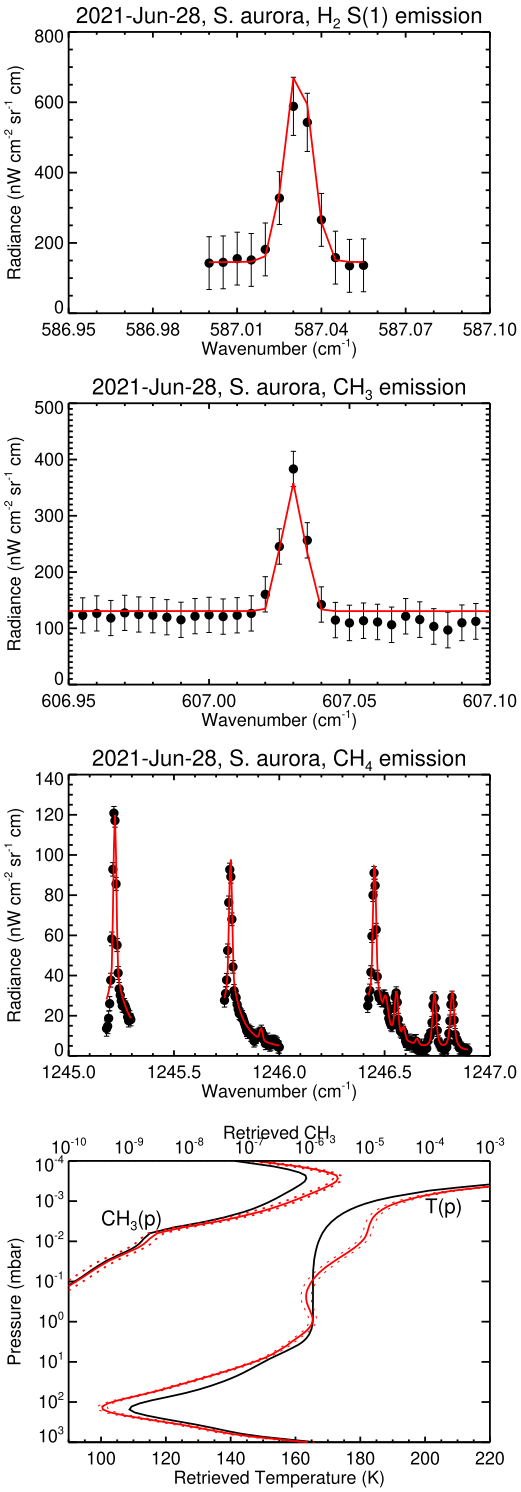

Figure 14. Observed IRTF-TEXES spectra (points with error bars) of the southern auroral H_2 S(1) (top panel), CH_3 (second panel), and CH_4 (third panel) emission as recorded by IRTF-TEXES on 2021 June 28. The best-fitted model spectrum is included as solid red. The bottom panel shows the corresponding retrieved profiles of temperature (according to the lower *x*-axis) and CH_3 volume mixing ratio (according to the upper *x*-axis).

homopause levels poleward of the northern MAE with the region equatorward but in the same latitude circle (i.e., comparing red and blue results in Figures 9 and 10). As noted previously, in performing such a comparison in the north, results can be split into three categories or "types":

1. *Type I*: there is negligible difference (with respect to uncertainty) in homopause level in both pressure and altitude space.
2. *Type II*: the homopause level poleward of the MAE is at a statistically significantly higher altitude compared to equatorward of the MAE, but there is negligible (within uncertainty) difference in homopause level in pressure space.
3. *Type III*: the homopause level poleward of the MAE is at both a statistically significant higher altitude and a statistically significant lower pressure compared to the homopause level equatorward of the MAE.

For Type I, our interpretation is that there is negligible difference in the rate of vertical transport between the regions poleward and equatorward of the MAE. We note that at these times/locations the retrieved temperature profiles (Figure 12) indicate an absence of strong auroral-related heating. For example, using results derived from IRTF-TEXES observations on 2021 November 8, there is negligible difference in homopause level between regions inside and outside of the auroral regions, and the retrieved temperature profile is relatively isothermal. We further consider the link between heating and homopause level in our discussions of Types II and III below.

For Type II, our interpretation in such cases is that there is negligible difference in the rate of vertical transport between regions poleward and equatorward of the MAE, but strong auroral-related heating in the former increases the atmospheric scale height such that the same homopause pressure level occurs at a higher altitude. This also highlights an important point in the context of adopting vertical hydrocarbon profiles in the quantitative analyses of Jupiter's ultraviolet auroral emissions. Ideally, the vertical hydrocarbon profiles should be adopted in pressure space. Adopting the vertical profiles in altitude space does not take into account the local temperature profile and its short-term temporal variability (see Figures 12 and 15).

For Type III, our interpretation is that there is enhanced vertical transport poleward of the MAE compared to the equatorward location. The exact source or sources of the enhanced vertical transport remain uncertain. We generally find that at the times/locations poleward of the MAE where enhanced vertical transport is inferred, there is stronger auroral-related heating (see Figures 12 and 15). As noted above for Type I, an absence of auroral-related heating leads to negligible difference in homopause level between regions poleward and equatorward of the MAE. This could suggest that the enhanced vertical transport is driven by similar processes that produce the heating and/or that the heating itself drives the enhanced vertical transport. We note that at times when there is a maximum in temperature at 1 mbar, the region immediately above this level is unstable to convection/upward advection (see, e.g., Figure 11). However, the atmosphere returns to an isothermal or positive lapse rate at pressures lower than ~0.1 mbar, and therefore such upward motions would likely extend over less than a decade of pressure. Three-dimensional and time-dependent circulation modeling of the polar atmosphere of Jupiter with a parameterization for auroral energy input is needed in order to better understand the connections between magnetospheric forcing and vertical motions.

6.1.2. Southern Auroral Region

Figure 13 shows derived homopause levels as a function of latitude and time at mid- to high southern latitudes. In order to test

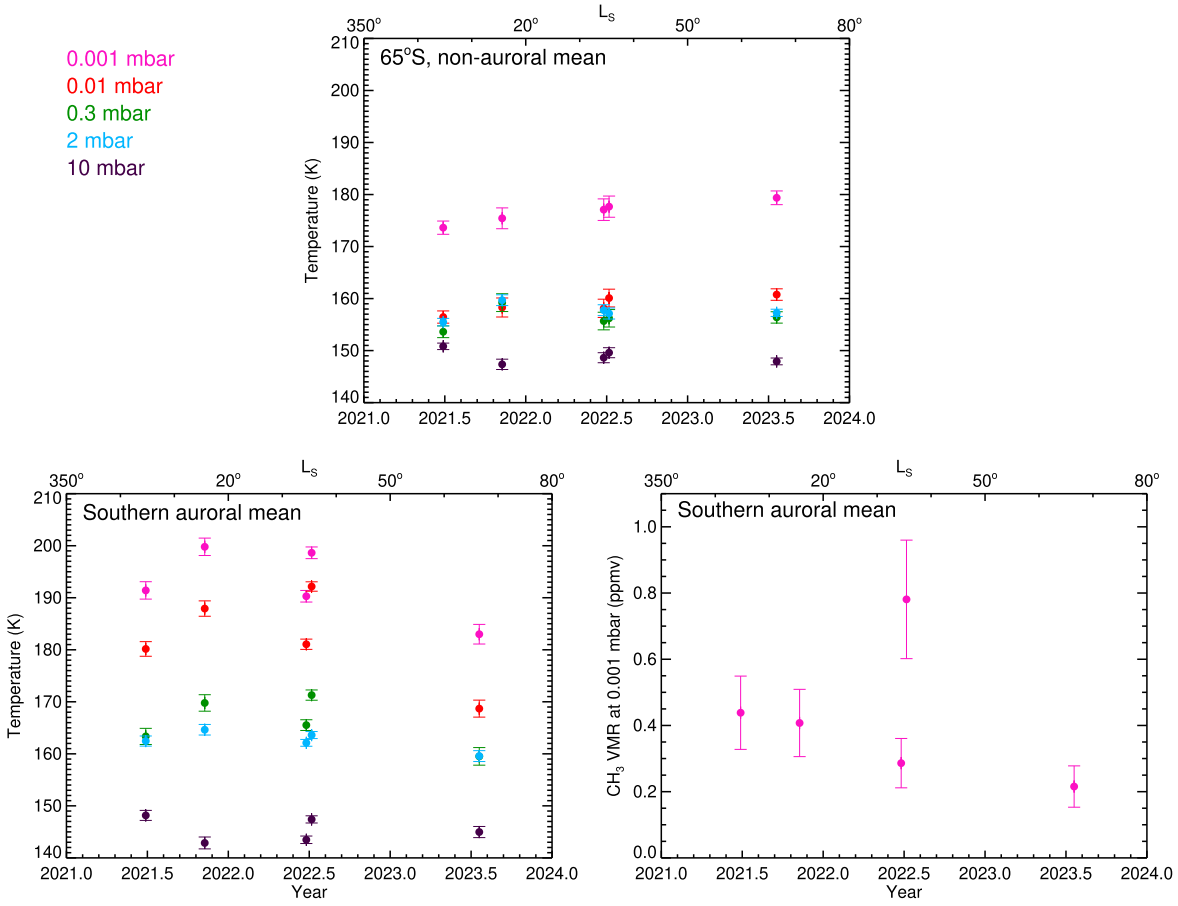

Figure 15. Top panel: retrieved temperature profiles (solid colored lines) and uncertainty (dotted colored lines) using the non-auroral-mean spectra at 65°S for IRTF-TEXES results. Results are colored according to the pressure level, as indicated by the legend on the left. The bottom left panel shows similar results for temperatures retrieved from the southern auroral-mean spectra (poleward of the MAE). The bottom right panel shows retrieved profiles of CH_3, which was allowed to vary in fitting the auroral-mean spectra. Only the 1 μbar results are shown where there is sensitivity to CH_3 (see Figure 7).

whether the region poleward of the southern MAE is subject to enhanced vertical transport, we compare derived homopause levels there with results derived equatorward at 65°S.

We find that for all dates presented in this work, derived homopause levels poleward of the southern MAE agree within uncertainty in both altitude and pressure space with those at 65°S. This implies that there is negligible difference in vertical transport between the southern auroral region and high southern latitudes outside the auroral region. However, we suggest that this is an artifact of the observations/analysis rather than a real result for the following reasons. First, the limited spatial resolution provided by IRTF's 3 m primary aperture, together with the highly foreshortened location of the southern auroral region on Jupiter, means that we could only sample the very edge of the region poleward of the southern MAE (Figure 1). It is possible that regions of enhanced vertical transport exist at regions further poleward of those resolvable from 3 m Earth-based telescopes. Second, results derived in the north (see Section 5.1 and our discussion in Section 6.1.1) suggest that higher homopause levels occur at times/locations where auroral-related heating is stronger. Using Gemini-TEXES observations recorded in 2017 March (J. A. Sinclair et al. 2023), which were able to resolve a larger proportion of the area poleward of the southern MAE, the regions of strongest heating occur poleward of the regions that could be sampled in this work. Third, P. Rodrìguez-Ovalle et al. (2024) performed a similar analysis of Mid-Infrared Instrument (MIRI; G. H. Rieke et al. 2015) medium-resolution spectra on JWST and determined that the homopause level was elevated poleward of the southern MAE. Differences in the results between this work and P. Rodrìguez-Ovalle et al. (2024) are discussed further in Section 6.4.

6.2. Variability in Temperature/CH_3

Equatorward of northern MAE at 62.5°N, temperatures exhibit an overall warming trend over the period from 2019 April (L_s ~ 300°) to 2023 July (L_s ~ 60°) (Figure 12). This is consistent with the increasing solar insolation at Jupiter's high northern latitudes as the subsolar latitude moved north of the equator in 2021 May (L_s ~ 0°). The radiative climate model of Jupiter presented in S. Guerlet et al. (2020) shows an ~8 K heating of the atmosphere at 10 mbar at 60°N in going from $L_s = 300°$ to 60° (see Figure 11 of their paper). This is consistent with the change in temperature observed at 62.5°N outside of or equatorward of the northern auroral region in this work (Figure 12).

At 60°S, the same radiative climate model (S. Guerlet et al. 2020) shows a marginal cooling of ~3 K at 10 mbar over the $L_s = 0°$–60° time period. This predicted change in temperature is comparable to our uncertainty on temperature changes: our results in Figure 15 show no significant changes in temperature with respect to uncertainty from 2021 June (L_s ~ 3°) to 2023 July (L_s ~ 60°). In general, S. Guerlet et al. (2020) show seasonal variations in temperature at 60°S to be relatively muted compared to those at 60°N. This is interpreted to result

from the hemispheric asymmetry in the density of polar haze particles, which originate predominantly from Jupiter's auroral regions, as the influx of charged particles increases the rate of their production (e.g., A.-S. Wong et al. 2000, 2003; A. J. Friedson et al. 2002). Aurorally produced haze particles absorb shortwave solar radiation and in turn heat the atmosphere. Given that the northern auroral region extends to relatively lower latitudes (~55°N) compared to the south (~68°S), the 10 mbar density of such haze particles is expected to be 4–10 times higher at 60°N compared to 60°S (X. Zhang et al. 2015; S. Guerlet et al. 2020), and thus heating/cooling rates are higher in the former compared to the latter.

Poleward of the southern and northern MAEs, temperature profiles exhibit erratic/random variability with time (Figures 12 and 15). Temperatures at 1 mbar and 0.01 mbar vary over a range of ~10 and ~25 K, respectively. Magnetospheric dynamics are driven by internal processes (Io's volcanic activity) or due to perturbations in the external solar wind environment. This in turn drives electrons and charged particles into the neutral atmosphere, where they ultimately deposit their energy as heat as deep as the 1–10 mbar level. These processes vary on timescales of hours to days, and thus temperatures poleward of the MAEs exhibit short-term variability.

Auroral-related heating occurs predominantly at two levels: ~1 mbar and lower than 0.1 mbar (e.g., J. A. Sinclair et al. 2018, 2023). Based on thermospheric circulation models of Jupiter's polar regions (e.g., S. W. Bougher et al. 2005; J. Yates et al. 2014), the heating at ~0.01 mbar is expected to be some combination of Joule heating and dynamical heating associated with ion drag. In past work where observations were binned such that temperatures were derived over several longitudinal points poleward of the MAE, the strongest upper-stratospheric heating is observed in a region centered poleward of the MAE (e.g., J. A. Sinclair et al. 2017b, J. A. Sinclair et al. 2018). Oddly, the strongest heating associated with ion drag would be expected nearer the MAE, where velocity shears are largest. Indeed, in limb viewing of Jupiter's high southern latitudes, the Doppler shift of CO lines indicated strong, narrow jets colocated with the southern MAE, which is inferred to result from spin-up of the neutral species by ion drag. The extent to which ion drag is responsible for the upper-stratospheric heating in the region centered poleward and away from the MAE is therefore uncertain. The source(s) of the 1 mbar auroral-related heating have similarly proven elusive: further discussion is given in Sections 6.1–6.2 of J. A. Sinclair et al. (2023). Here we suggest a hypothesis for the 1 mbar auroral-related heating not discussed in previous work. As detailed in W. Xu et al. (2018; albeit for Earth's space weather), energetic electron precipitation in the upper atmosphere produces bremsstrahlung photons, which then produce a secondary ionization peak in the deeper atmosphere through Compton scattering and the photoelectric effect. Such a phenomenon may even have been observed by Juno's MWR (M. A. Janssen et al. 2017): 600 MHz brightness temperatures are cooler over Jupiter's auroral regions, which are interpreted to result from a layer of reflecting and absorbing plasma in the lower stratosphere (A. Bhattacharya et al. 2025). Precipitation modeling, which captures secondary ionization by bremsstrahlung, would be required to test this hypothesis. In order to understand the interplay between dynamics directly driven by the aurora (through ion drag), different sources of auroral heating, and the dynamics resulting from auroral heating, time-dependent circulation modeling of Jupiter's polar stratosphere is required.

In spectra equatorward of the MAE, we found that the emission features of CH_3 and CH_4 could be fit sufficiently by adopting the photochemically predicted vertical profiles of each species and only allowing temperature to vary. In spectra poleward of the MAE, we had to allow the vertical profile of CH_3 to vary in order to fit its emission feature within the noise. We consider this a result of uncertainties in the CH_3 chemical kinetics (e.g., M. Dobrijevic et al. 2003; M. Dobrijevic et al. 2010), or an additional source of CH_3 production in the auroral regions not included in the photochemical model, or a combination of both. Figures 12 and 15 show retrieved abundances of CH_3 poleward of the northern and southern MAE as a function of time. Temporal variability in CH_3 abundances appears generally insignificant owing to the larger uncertainties; therefore, we cannot rule out temporal variability by magnitudes smaller than ~25%. The exception is the CH_3 abundance derived poleward of the southern MAE on 2022 July 6. Both upper-stratospheric temperatures and CH_3 abundances are elevated on this date in comparison to the results ~12 days earlier on June 24. This suggests the response of the atmosphere to a transient, energetic event intermediate of the June 24 and July 6 measurements.

6.3. Comparison of IRTF-TEXES and SOFIA-EXES Results

Homopause levels derived from SOFIA-EXES have smaller uncertainties than those derived from IRTF-TEXES. EXES's bandpass at 1299 cm^{-1} samples a greater number of strong emission lines of CH_4, which extends the vertical range of sensitivity to higher altitudes/lower pressures compared to the IRTF, which has a shorter bandpass at 1245 cm^{-1} with a lower density of strong CH_4 lines (see Figure 7). The SOFIA-EXES data therefore have an overall higher sensitivity to the altitudes at which CH_3 and CH_4 vary in response to changes in the eddy diffusion. Unfortunately, SOFIA has been decommissioned, and so similar observations are not possible in the future. IRTF-TEXES could target the 1299 cm^{-1} spectral range but would require longer exposure times to achieve similar sensitivities.

Poleward of the northern MAE, temperature profiles retrieved from SOFIA-EXES observations exhibit an inflection point at the ~5 mbar level (see Figure 11). This contrasts the shape of profiles retrieved from IRTF-TEXES (Figures 14; J. A. Sinclair et al. 2018, 2020, 2023), where there is generally a maximum in temperature at ~1 mbar. Either the difference in shape is a real feature resulting from temporal variability of the temperature profile between measurements, or the analysis of SOFIA-EXES data results in a different vertical sensitivity in the atmosphere compared to that of IRTF-TEXES data. We favor the former explanation and tentatively rule out the latter as justified below. First, Figure 7(e) shows the vertical contribution functions of both SOFIA-EXES and IRTF-TEXES, and both data sets are sufficiently sensitive to the atmosphere between 50 and 0.1 mbar and therefore should converge on the same temperature profile over this pressure range. We also considered the fact that inversions of IRTF-TEXES observations include the H_2 S(1) quadrupole feature at 587.03 cm^{-1} (e.g., Figures 2, 14), which sounds the atmosphere from ~50 to ~1 mbar (see Figure 4 of J. A. Sinclair et al. 2020), whereas this feature/spectral setting was not measured by EXES. However, in Appendix C we tested and compared temperature retrievals from IRTF-TEXES spectra both including and omitting the H_2 S(1) feature and found negligible difference in the shape/magnitude of the temperature profile. We therefore also rule out that the inclusion/omission of the H_2 S(1) feature leads to largely different temperature profiles.

6.4. Comparison with Previous Studies

This work serves as an extension of J. A. Sinclair et al. (2020), but with the following improvements. First, we perform the analysis over an updated photochemical model grid (based on the model presented in J. I. Moses & A. R. Poppe 2017). The grid uses a larger range in homopause pressure/eddy diffusion coefficient (see Figure 6) compared to that in J. A. Sinclair et al. (2020). The updated grid also uses model output at 60°N, compared to 30°N in J. A. Sinclair et al. (2020), which is more appropriate for this study, which focuses on mid- to high latitudes. In Appendix B, using IRTF-TEXES observations recorded on 2019 August 20, we directly compare derived homopause levels using the updated model grid of this work with the older grid used in J. A. Sinclair et al. (2020). In summary, we find that for a subset of locations/times the new model grid was able to better constrain 1σ lower limits on homopause levels, whereas the older grid could only determine an upper limit. In general, derived homopause levels exhibited negligible change with respect to uncertainty in using the older versus newer model grid.

In general, we find that Models 8b and 9b (Figures 6) optimize the simultaneous fit to the CH_3 and CH_4 spectral emission features in observations recorded poleward of the MAE. This corresponds to eddy diffusion coefficients in a range from $10 \times 10^6\,cm^2\,s^{-1}$ to $23 \times 10^6\,cm^2\,s^{-1}$ (see Figure 6) in this region, with upper-limit uncertainties of approximately $50 \times 10^6\,cm^2\,s^{-1}$. These are consistent with an analysis of Cassini-UVIS (C. D. Parkinson et al. 2006) observations of Jupiter's 587 Å helium airglow, where the eddy diffusion coefficients at Jupiter's auroral regions were concluded to be at least $8 \times 10^6\,cm^2\,s^{-1}$ and possibly larger than $40 \times 10^6\,cm^2\,s^{-1}$. In comparison, the same study derived an eddy diffusion coefficient of $2 \times 10^6\,cm^2\,s^{-1}$ at Jupiter's equatorial latitudes.

P. Rodrìguez-Ovalle et al. (2024) presented medium-resolution ($1460 < R < 3750$) JWST-MIRI observations JWST of Jupiter's high southern latitudes recorded in 2022 December as part of the Early Release Science 1373 program (PI: Imke de Pater). The primary aperture of JWST is 6.5 m and therefore achieves a higher diffraction-limited spatial resolution than the observations presented in this work. The JWST-MIRI spectra were therefore able to resolve several locations poleward of the southern MAE. P. Rodrìguez-Ovalle et al. (2024) inverted their spectra over the same photochemical model grid used in this work (Figure 6) but instead used the ν_2 and ν_4 bands of CH_4 (~1540 and ~1300 cm^{-1}, respectively) in order to retrieve stratospheric temperatures and the homopause level. They determined that the CH_4 homopause poleward of the southern MAE was 590^{+25}_{-118} km above 1 bar, in comparison to an upper limit of 350 km equatorward of the MAE. These results are consistent within uncertainty with the results of this work. For example, using IRTF-TEXES measurements recorded on 2021 November 8 (data closest in time to those of JWST), we derive a CH_4 homopause altitude of 404^{+170}_{-44} km poleward of the southern MAE and 360^{+25}_{-26} km at 65°S (representative of a lower latitude). The uncertainties derived on homopause altitudes in P. Rodrìguez-Ovalle et al. (2024) were smaller such that they were able to conclude that the altitude poleward of the southern MAE was elevated above uncertainty with respect to that derived equatorward of the southern MAE. We attribute the improved sensitivity to CH_4 homopause altitude in P. Rodrìguez-Ovalle et al. (2024) compared to this work for two reasons. First, JWST-MIRI achieves very high SNRs in radiance (e.g., G. H. Rieke et al. 2015), which results in improved discrimination between models. Second, JWST has a larger primary aperture (6.5 m) compared to the IRTF (3 m), which results in higher diffraction-limited spatial resolutions, and therefore a larger number of spectra poleward of the southern MAE to coadd, further augmenting JWST-MIRI's superior sensitivity. Third, JWST-MIRI spectra measure the Q-branch of the ν_4 band, which sounds higher altitudes.

Z. L. Brown et al. (2024) derived homopause levels as a function of latitude and time on Saturn using a simultaneous analysis of Cassini Ion Neutral Mass Spectrometer (INMS; J. H. Waite et al. 2004), Composite Infrared Spectrometer (CIRS; V. G. Kunde et al. 1996), and Ultraviolet Imaging Spectrograph (UVIS; L. W. Esposito et al. 2004) observations. Comparative planetology between Jupiter and Saturn can be determined by comparing the results of their study with this work. Z. L. Brown et al. (2024) found that the homopause pressure on Saturn varied from $\log(50\ \text{nbar}) = 1.7$ at equatorial latitudes to $\log(5000\ \text{nbar}) = 3.7$ at the poles. Thus, the homopause level on Saturn is over a decade of pressure deeper than that derived for Jupiter ($\log(p_H(\text{nbar}) \sim 2.1$). On Saturn, the trend of higher homopause at equatorial latitudes and deeper homopause at higher latitudes was interpreted to be driven by upwelling at the former and downwelling at the latter. The equator-to-pole trend in homopause level on Saturn is therefore the opposite of what is observed on Jupiter in this work and previous work (C. D. Parkinson et al. 2006; G. Clark et al. 2018; J. A. Sinclair et al. 2020; P. Rodrìguez-Ovalle et al. 2024). This demonstrates the power of magnetospheric forcing on Jupiter and its ability to modulate the structure and dynamics of the neutral atmosphere to a much greater extent than a similar giant planet with a weaker magnetic field.

6.5. Future Work

For a given location, derived homopause levels have larger uncertainties in the direction of the top of the atmosphere (i.e., the lower uncertainty in pressure units, the upper uncertainty in altitude units). This is because the observations have limited sensitivity to the atmosphere at pressures lower than 0.1 μbar (Figure 7). Thus, no interpretation of temporal variability can be made in comparing absolute homopause levels at a given location as a function of time. However, the fact that the results fall into Types I, II, and III above, as well as the fact that a given location can change between Types I, II, and III as a function of time, does tentatively suggest that there is temporal variability of homopause level poleward of the northern MAE. Uncertainties on derived homopause levels would need to be decreased in order for temporal variations to be assessed directly. As noted above, a coupled analysis of INMS, CIRS, and UVIS observations by Cassini was able to constrain homopause levels on Saturn with high precision (Z. L. Brown et al. 2024); a similar analysis of contemporaneous mid-infrared and ultraviolet spectra of Jupiter may also allow the homopause to be constrained to a higher precision.

The mid-infrared observations used in this study are diffraction limited in spatial resolution, and coaddition of several individual spectra is required to increase the effective SNR to a sufficient level for radiative transfer analysis. These limitations meant that observations in the north had to be coadded over large spatial ranges (see Figure 1) such that we can only compare homopause levels poleward and equatorward of the northern MAE. The limited spatial resolution and the highly foreshortened location of the southern MAE from Earth mean that only the very edge of the region poleward of the MAE can be resolved. Similar TEXES

observations to those presented in this work but recorded on Gemini-North would achieve 2.5–3 times higher spatial resolutions owing to Gemini's 8 m primary compared to the 2.5–3 m primary of IRTF/SOFIA. While Gemini-North/TEXES observations were presented in J. A. Sinclair et al. (2023), these did not include the 606 cm^{-1} spectral setting necessary to record CH_3 emission and perform the analysis presented in this work. Gemini-TEXES observations would allow more poleward areas of the southern auroral region to be resolved. The spatial resolutions achieved at high southern latitudes could be marginally improved further by observing when the subobserver latitude is at its most southern extent (~3.8°S): the next such window is in the 2029–2030 time period at the time of writing. Significant improvements to the spatial resolutions could be achieved with future, mid-infrared spectroscopy on the Extremely Large Telescope/Thirty Meter Telescope (ELT/TMT) with primary apertures $\geqslant$30 m or a future mission with a polar orbiter.

7. Conclusions

We performed radiative transfer analyses of IRTF-TEXES and SOFIA-EXES spectra recorded between 2019 April 16 and 2023 July 20. The spectral emission features of H_2 S(1) (hydrogen quadrupole), CH_3 (methyl radical), and CH_4 (methane) were mapped across Jupiter's mid- to high latitudes and coadded to sample regions inside (or magnetospherically poleward) of and outside (or magnetospherically equatorward) of the ultraviolet MAEs. The coadded spectra were then inverted across a grid of photochemical models of varying eddy diffusion coefficients/homopause pressures. The quality of fit of the synthetic spectra to the observed spectra was used to derive the best-fitting homopause pressure, and the retrieved temperature–pressure profile was used to convert the homopause pressure to an altitude with respect to 1 bar. The goal was to assess whether the regions poleward of the ultraviolet MAEs are subject to enhanced vertical transport. A second goal was to constrain the location of the CH_4 homopause level to support investigations of Jupiter's ultraviolet auroral emissions by Juno, Hubble, and Hisaki, for which the vertical hydrocarbon profiles are a source of uncertainty. Listed below are our conclusions.

1. For a subset of latitudes and times, derived homopause levels poleward of the northern MAE are at a statistically significantly lower pressure and higher altitude compared to regions equatorward of the northern MAE. We derive eddy diffusion coefficients in a range from 10×10^6 cm^2 s^{-1} to 23×10^6 cm^2 s^{-1} poleward of the northern MAE compared to an upper limit of $<1 \times 10^6$ cm^2 s^{-1} derived at lower latitudes. Thus, the region poleward of the northern MAE is subject to enhanced vertical transport compared to elsewhere on the planet.
2. For a further subset of latitudes and times, derived homopause levels poleward and equatorward of the northern MAE agree within uncertainty in pressure but are at a statistically significant higher altitude in the former. For such locations/times, we interpret similar rates of vertical transport between the two regions, but auroral-related stratospheric heating and the resulting increased scale height poleward of the northern MAE place the homopause at a higher altitude compared to the latter.
3. For remaining latitudes/times, there was no significant difference in homopause level (in either altitude or pressure) between regions poleward and equatorward of the northern MAE.
4. The range of results noted above could tentatively suggest that the CH_4 homopause level is spatially and temporally variable poleward of the northern MAE or could simply be a result of variable uncertainties as a function of latitude and time.
5. Derived homopause levels poleward of the southern MAE are in agreement within uncertainty with those derived equatorward of the southern MAE. We favor this result being an artifact of spatial sampling rather than an indication that the region poleward of the southern MAE is not subject to enhanced vertical transport.

Acknowledgments

The research was carried out at the Jet Propulsion Laboratory, California Institute of Technology, under a contract with the National Aeronautics and Space Administration (80NM0018D0004). The material is based on work supported by NASA under grants NNH17ZDA001N and NNH20ZDA001N issued through the Solar System Observations Planetary Astronomy program. A subset of the observations presented in this work were recorded at NASA's Infrared Telescope Facility (IRTF). The IRTF is operated by the University of Hawaii under contract 80HQTR19D0030 with NASA. A subset of the observations presented in this work were recorded with the NASA/DLR Stratospheric Observatory for Infrared Astronomy (SOFIA) during Cycles 7 and 8. SOFIA is jointly operated by the Universities Space Research Association, Inc. (USRA), under NASA contract NNA17BF53C, and the Deutsches SOFIA Institut (DSI) under DLR contract 50 OK 2002 to the University of Stuttgart. Financial support for this work was provided by NASA through award nos. 07_0222 and 08_219 issued by USRA. The radiative transfer analyses presented in this work were performed efficiently using JPL's High Performance Computing (HPC) resources, which were provided by funding from the JPL Information and Technology Solutions Directorate. We also thank both reviewers for their helpful and constructive feedback.

Facilities: SOFIA, IRTF

Software: NEMESIS (P. G. J. Irwin et al. 2008).

Data Availability Statement

Raw and processed forms of both the IRTF-TEXES and SOFIA-EXES observations presented in this work are publicly available at the Infrared Science Archive, IRSA.[12] However, spatially mapped and absolutely calibrated versions of both sets of observations can be requested from the authors. The NEMESIS radiative transfer code is available on GitHub.[13]

Appendix A
Observation Details

A.1. IRTF-TEXES

Table A1 provides details of the IRTF-TEXES observations adopted in this work.

[12] https://irsa.ipac.caltech.edu/frontpage/

[13] https://github.com/nemesiscode/radtrancode

Table A1
Details of IRTF-TEXES Observations

Date	Time (UTC)	Scan Number	Setting (cm^{-1})	R	Slit (arcsec)	N_{spx}	Hem.	CML (deg)	SOL (deg)	A	v_{rad} (km s^{-1})
2019 Apr 16	11:14	2010.01	1248	80000	10.6 × 1.4	927	N	111	−3.1	2.12	−24.2
	11:14	2010.02	1248	80000	10.6 × 1.4	669	N	111	−3.1	2.12	−24.2
	11:20	2011.01	1248	80000	10.6 × 1.4	437	N	113	−3.1	2.05	−24.2
	11:20	2011.02	1248	80000	10.6 × 1.4	87	N	113	−3.1	2.05	−24.2
	11:26	2012.01	1248	80000	10.6 × 1.4	420	N	115	−3.1	1.99	−24.2

Note. Dates/times are UTC; R ($=\nu/\Delta\nu$) is the spectral resolving power; the slit dimensions (length × width) are in arcseconds; "Hem.," short for hemisphere, indicates whether the scan was over mid- to high northern or southern latitudes, indicated by "N" or "S," respectively. The central meridian longitude (CML) at the time of scan is System III, and the subsolar latitude (SOL) is planetocentric. A is the mean air mass throughout the scan, and v_{rad} is the relative Earth–Jupiter velocity.
(This table is available in its entirety in machine-readable form in the online article.)

A.2. SOFIA-EXES

Table A2 provides details of the SOFIA-EXES observations adopted in this work.

Table A2
Details of SOFIA-EXES Observations

Date	Time (UTC)	Scan Number	Setting (cm^{-1})	R	Slit (arcsec)	N_{spx}	Hem.	CML (deg)	SOL (deg)	A	v_{rad} (km s^{-1})
	08:55	30064	606	66667	19.5 × 2.4	840	N	191	0.2	2.06	−26.4
	08:59	30065	606	66667	19.5 × 2.4	456	S	193	0.2	1.99	−26.4
	09:03	30066	606	66667	19.5 × 2.4	399	S	209	0.2	1.96	−26.4
	09:06	30067	606	66667	19.5 × 2.4	553	S	210	0.2	1.94	−26.4
	09:13	30069	1299	85714	11.0 × 1.8	468	N	212	0.2	1.91	−26.4
2021-Jun-10	09:18	30070	1299	85714	11.0 × 1.8	530	N	214	0.2	1.86	−26.4
	09:28	30072	1299	85714	11.0 × 1.8	382	S	218	0.2	1.82	−26.4
	09:47	30077	606	66667	19.5 × 2.4	972	N	224	0.2	1.71	−26.4
	09:50	30078	606	66667	19.5 × 2.4	467	S	226	0.2	1.71	−26.4
	09:59	30081	1299	85714	11.0 × 1.8	571	N	229	0.2	1.66	−26.4
	10:04	30082	1299	85714	11.0 × 1.8	378	S	231	0.2	1.64	−26.4
	09:48	40058	606	66667	19.5 × 2.4	543	S	15	0.2	1.85	−26.2
	09:50	40059	606	66667	19.5 × 2.4	557	S	16	0.2	1.84	−26.2
	09:53	40060	606	66667	19.5 × 2.4	789	N	17	0.2	1.80	−26.2
	09:55	40061	606	66667	19.5 × 2.4	760	N	18	0.2	1.82	−26.2
	10:01	40063	1299	85714	11.0 × 1.8	427	S	20	0.2	1.81	−26.2
	10:05	40064	1299	85714	11.0 × 1.8	362	N	22	0.2	1.77	−26.2
	10:09	40065	1299	85714	11.0 × 1.8	407	N	23	0.2	1.79	−26.2
	10:26	40070	606	66667	19.5 × 2.4	990	N	44	0.2	1.70	−26.2
	10:28	40071	606	66667	19.5 × 2.4	558	S	44	0.2	1.68	−26.2
2021-Jun-11	10:31	40072	606	66667	19.5 × 2.4	848	N	46	0.2	1.68	−26.2
	10:36	40074	1299	85714	11.0 × 1.8	494	S	47	0.2	1.65	−26.2
	10:41	40075	1299	85714	11.0 × 1.8	398	N	49	0.2	1.64	−26.2
	10:45	40076	1299	85714	11.0 × 1.8	501	N	51	0.2	1.62	−26.2
	11:03	40082	606	66667	19.5 × 2.4	429	S	72	0.2	1.58	−26.2
	11:05	40083	606	66667	19.5 × 2.4	615	S	72	0.2	1.57	−26.2
	11:07	40084	606	66667	19.5 × 2.4	788	N	73	0.2	1.57	−26.2
	11:12	40086	1299	85714	11.0 × 1.8	486	S	75	0.2	1.56	−26.2
	11:16	40087	1299	85714	11.0 × 1.8	412	N	76	0.2	1.55	−26.2
	11:20	40088	1299	85714	11.0 × 1.8	506	N	78	0.2	1.53	−26.2
	08:27	70042	606	66667	19.5 × 2.4	1268	N	155	0.2	2.05	−25.2
	08:30	70043	606	66667	19.5 × 2.4	663	S	156	0.2	2.01	−25.2
	08:32	70044	606	66667	19.5 × 2.4	522	S	157	0.2	2.02	−25.2
	08:33	70045	606	66667	19.5 × 2.4	664	S	157	0.2	1.98	−25.2
	08:36	70046	606	66667	19.5 × 2.4	1302	N	158	0.2	1.96	−25.2
	08:50	70048	1299	85714	11.0 × 1.8	567	N	163	0.2	1.87	−25.2
2021-Jun-17	08:54	70049	1299	85714	11.0 × 1.8	550	N	165	0.2	1.86	−25.2
	08:59	70050	1299	85714	11.0 × 1.8	391	S	167	0.2	1.82	−25.2
	09:13	70055	606	66667	19.5 × 2.4	834	N	186	0.2	1.75	−25.2

Table A2
(Continued)

Date	Time (UTC)	Scan Number	Setting (cm^{-1})	R	Slit (arcsec)	N_{spx}	Hem.	CML (deg)	SOL (deg)	A	v_{rad} ($km\ s^{-1}$)
	09:15	70056	606	66667	19.5 × 2.4	537	S	187	0.2	1.74	−25.2
	09:18	70057	1299	85714	11.0 × 1.8	393	N	188	0.2	1.70	−25.2
	09:22	70058	1299	85714	11.0 × 1.8	467	N	190	0.2	1.71	−25.2
	09:26	70059	1299	85714	11.0 × 1.8	443	S	191	0.2	1.69	−25.2
	08:16	80038	606	66667	19.5 × 2.4	655	N	302	0.2	1.87	−25.0
	08:19	80039	606	66667	19.5 × 2.4	874	N	303	0.2	1.86	−25.0
	08:22	80040	606	66667	19.5 × 2.4	473	S	304	0.2	1.82	−25.0
	08:24	80041	606	66667	19.5 × 2.4	574	S	305	0.2	1.82	−25.0
	08:29	80043	1299	85714	11.0 × 1.8	504	N	306	0.2	1.79	−25.0
	08:33	80044	1299	85714	11.0 × 1.8	552	N	308	0.2	1.75	−25.0
	08:37	80045	1299	85714	11.0 × 1.8	313	S	309	0.2	1.75	−25.0
	08:51	80050	606	66667	19.5 × 2.4	951	N	314	0.2	1.70	−25.0
	08:53	80051	606	66667	19.5 × 2.4	392	S	315	0.2	1.66	−25.0
	08:58	80053	1299	85714	11.0 × 1.8	446	N	317	0.2	1.64	−25.0
	09:02	80054	1299	85714	11.0 × 1.8	505	N	318	0.2	1.62	−25.0
	09:06	80055	1299	85714	11.0 × 1.8	354	S	320	0.2	1.60	−25.0
	09:21	80061	606	66667	19.5 × 2.4	951	N	340	0.2	1.55	−25.0
2021-Jun-18	09:24	80062	606	66667	19.5 × 2.4	482	S	341	0.2	1.53	−25.0
	09:28	80064	1299	85714	11.0 × 1.8	415	N	342	0.2	1.52	−25.0
	09:33	80065	1299	85714	11.0 × 1.8	489	N	344	0.2	1.51	−25.0
	09:37	80066	1299	85714	11.0 × 1.8	330	S	346	0.2	1.50	−25.0
	09:40	80067	1299	85714	11.0 × 1.8	326	S	347	0.2	1.48	−25.0
	10:51	80079	606	66667	19.5 × 2.4	866	N	27	0.2	1.52	−25.0
	10:54	80080	606	66667	19.5 × 2.4	965	N	28	0.2	1.52	−25.0
	10:57	80081	606	66667	19.5 × 2.4	467	S	29	0.2	1.51	−25.0
	10:59	80082	606	66667	19.5 × 2.4	655	S	30	0.2	1.50	−25.0
	11:01	80083	606	66667	19.5 × 2.4	513	S	31	0.2	1.51	−25.0
	11:06	80085	1299	85714	11.0 × 1.8	294	N	32	0.2	1.50	−25.0
	11:10	80086	1299	85714	11.0 × 1.8	403	S	34	0.2	1.49	−25.0
	11:13	80087	1299	85714	11.0 × 1.8	433	S	35	0.2	1.52	−24.9
	11:24	80091	606	66667	19.5 × 2.4	492	S	53	0.2	1.46	−24.9
	11:26	80092	606	66667	19.5 × 2.4	473	S	54	0.2	1.46	−24.9
	11:30	80094	1299	85714	11.0 × 1.8	437	S	56	0.2	1.47	−24.9

Note. Dates/times are UTC; R ($=\nu/\Delta\nu$) is the spectral resolving power; the slit dimensions (length × width) are in arcseconds; "Hem.," short for hemisphere, indicates whether the scan was over mid- to high northern or southern latitudes, indicated by "N" or "S," respectively. The central meridian longitude (CML) at the time of scan is System III, and the subsolar latitude (SOL) is planetocentric. A is the mean air mass throughout the scan, and v_{rad} is the relative Earth–Jupiter velocity.

Appendix B
Comparison of Old versus New Model Grid

Using the IRTF-TEXES observations recorded on 2019 August 20, the analysis and derivation of homopause levels are performed using the older model grid presented in J. A. Sinclair et al. (2020). The results are presented in Figure B1 and compared with those presented in this work using the updated model grid (see Section 4.2 and Figure 6) to assess how derived homopause levels were affected by the change in model grid.

Overall, there is negligible change in homopause altitude with respect to uncertainty in using the older versus newer model grid. For a subset of non-auroral-mean results, using the extended model grid presented in this work allowed us to derive a best-fitting homopause altitude and lower and upper confidence levels, whereas only an upper limit could be derived using the model grid used in J. A. Sinclair et al. (2020). This is demonstrated in Figure B2, which shows variations in the χ^2 (Equation (1)) to the 60°N non-auroral-mean observation on 2019 August 20 using both model grids. Using the Sinclair+2020 models, Model 3 (~165.3 nbar homopause) minimizes χ^2, which corresponds to 345 km above 1 bar. In interpolating the variation in χ^2 as a function of homopause altitude toward higher altitudes, we derive an upper 1σ confidence level of 371 km. However, there is insufficient variation in χ^2 toward lower homopause altitudes in order to derive a lower confidence level, with Model 1 corresponding to $\chi^2_{min} + 0.9$. However, in using the newer model grid adopted in this work, we derive a CHA of 345 km above 1 bar, with lower and upper 1σ confidence levels of 326 and 362 km, respectively.

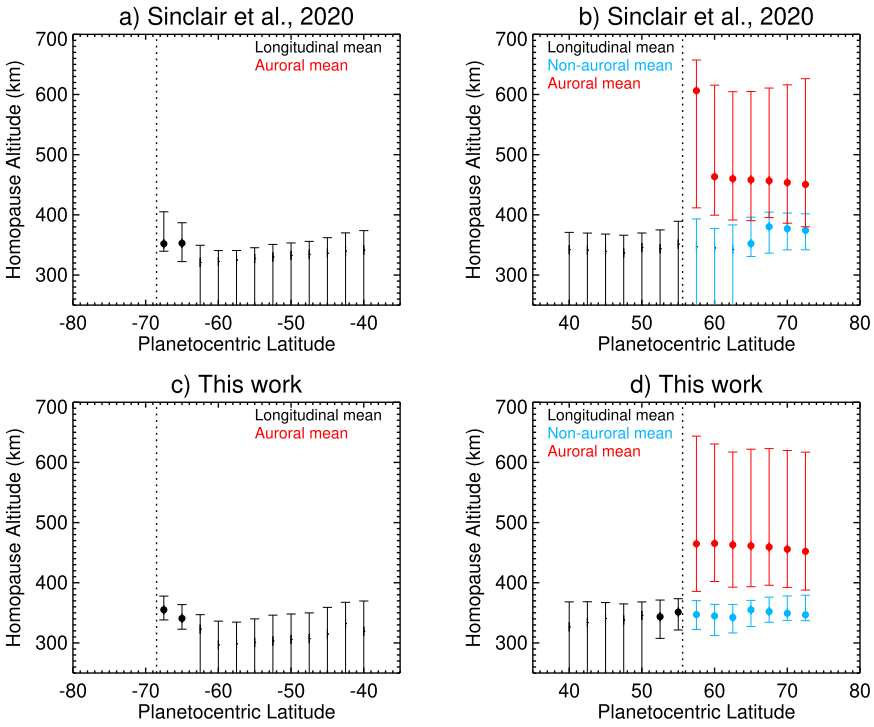

Figure B1. CH_4 homopause altitudes as a function of latitude, as derived from IRTF-TEXES observations on 2019 August 20. Results in the southern and northern hemispheres are shown on the left and right, respectively. The top row shows results previously presented in J. A. Sinclair et al. (2020) using an earlier model grid; the bottom row shows results derived in this work using the updated model grid (see Section 4.2 for further details). Black results denote a longitudinal mean where all sampled longitudes were coadded into a single spectrum. Blue results at high northern latitudes denote the nonauroral mean, where spectra recorded at longitudes outside/equatorward of the MAE were coadded into a single spectrum. Red results denote an auroral mean using observations inside or poleward of the MAE. Results that only shown an upper error bar are where a lower 1σ uncertainty could not be derived and so we show only an upper (1σ) limit. Vertical dashed lines mark the lowest-latitude extent of the southern and northern MAEs (B. Bonfond et al. 2017).

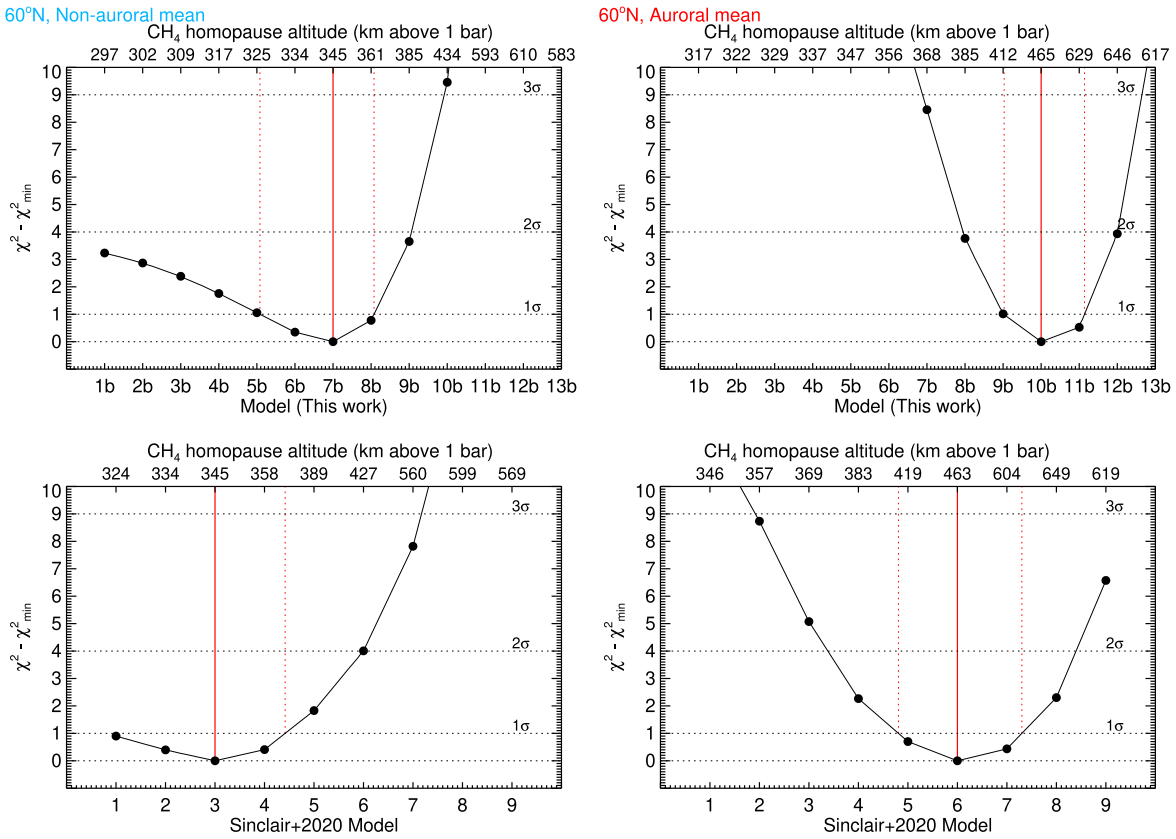

Figure B2. Variations in the χ^2 (Equation (1)) as a function of the model tested in fitting the non-auroral-mean observation (left column) and auroral-mean (right column) observation at 60°N on 2019 August 20. Results in the top row use the model grid presented in this work (Figure 6); results in the bottom row use the model grid presented in J. A. Sinclair et al. (2020). The conversion from homopause pressure of each model to altitude with respect to 1 bar is shown in the upper *x*-axis of each panel. Vertical solid and dotted red lines denote the best-fitting result and the 1σ confidence levels, respectively.

Appendix C
Testing the Omission of the H_2 S(1) Feature

As noted in Sections 3 and 4, SOFIA-EXES measurements did not include the 587 cm^{-1} spectral setting and therefore did not measure the H_2 S(1) quadrupole line feature, in contrast to those of IRTF-TEXES. In this appendix, we explore whether the omission of the hydrogen quadrupole line at 587.03 cm^{-1} significantly affected the retrieved temperature profile. In particular, we wanted to determine whether the absence of a local temperature maximum at ~1 mbar in SOFIA-EXES results poleward of the main oval could be explained by the omission of the H_2 S(1) feature.

We adopted the spectra recorded at 60°N by IRTF-TEXES on 2019 August 20 both poleward and equatorward of the main oval as two test cases. We repeated the analysis described in Section 4 but omitting the 587.03 cm^{-1} spectral setting. Figure C1 compares the retrieved temperature profiles including and omitting the H_2 S(1) feature in both locations.

We find that the omission or inclusion of the 587 cm^{-1} spectral setting has little effect on the retrieved temperature profile, both poleward and equatorward of the main oval. We also find that the 1 mbar auroral-related heating is present in the retrieved temperature profile regardless of whether the 587 cm^{-1} spectral setting is included or not. We therefore conclude that the omission of the H_2 S(1) feature from SOFIA-EXES retrievals cannot explain the absence of a local temperature maximum at the ~1 mbar level in SOFIA-EXES results.

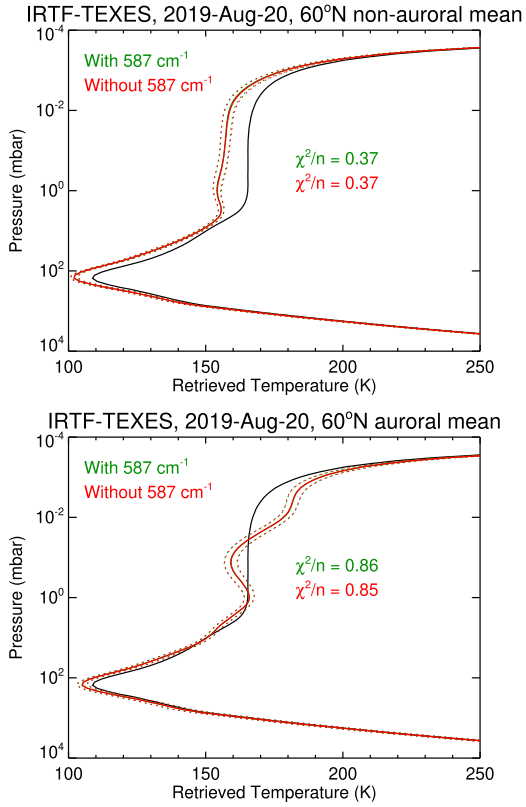

Figure C1. Retrieved temperature profiles using the non-auroral-mean (top panel) and auroral-mean (bottom panel) observations at 60°N. The black solid line indicates the a priori temperature profile; solid colored lines show retrieved profiles, with the uncertainty shown as a dotted line. Green results correspond to the inversion where the 587, 606, and 1248 cm^{-1} spectral settings were used; red results correspond to the inversion where the 587 cm^{-1} spectral setting was omitted. The reduced χ^2 values for each retrieval are indicated in each plot.

ORCID iDs

James A. Sinclair https://orcid.org/0000-0001-5374-4028
Thomas K. Greathouse https://orcid.org/0000-0001-6613-5731
Rohini S. Giles https://orcid.org/0000-0002-7665-6562
Matthew Richter https://orcid.org/0000-0002-8594-2122
Maisie Rashman https://orcid.org/0000-0002-3936-2469
Curtis de Witt https://orcid.org/0000-0002-6528-3836
Julianne Moses https://orcid.org/0000-0002-8837-0035
Vincent Hue https://orcid.org/0000-0001-9275-0156
Pablo Rodríguez-Ovalle https://orcid.org/0000-0003-2594-2128
Thierry Fouchet https://orcid.org/0000-0001-9040-8285
Ananyo Bhattacharya https://orcid.org/0000-0003-1898-8080
Bilal Benmahi https://orcid.org/0000-0002-2323-9968
Glenn S. Orton https://orcid.org/0000-0001-7871-2823
Leigh N. Fletcher https://orcid.org/0000-0001-5834-9588
Patrick G. J. Irwin https://orcid.org/0000-0002-6772-384X

References

Bhattacharya, A., Waite, J. H., Levin, S., et al. 2025, JGRA, submitted
Becker, H. N., Santos-Costa, D., Jørgensen, J. L., et al. 2017, GeoRL, 44, 4481
Bézard, B., Lellouch, E., Strobel, D., Maillard, J.-P., & Drossart, P. 2002, Icar, 159, 95
Bonfond, B., Saur, J., Grodent, D., et al. 2017, JGRA, 122, 7985
Bougher, S. W., Waite, J. H., Majeed, T., & Gladstone, G. R. 2005, JGRE, 110, E04008
Brown, Z. L., Koskinen, T. T., Moses, J. I., & Guerlet, S. 2024, Icar, 417, 116133
Cavalié, T., Benmahi, B., Hue, V., et al. 2021, A&A, 647, L8
Clark, G., Mauk, B. H., Haggerty, D., et al. 2017, GeoRL, 44, 8703
Clark, G., Tao, C., Mauk, B. H., et al. 2018, JGRA, 123, 7554
Dobrijevic, M., Cavalié, T., Hébrard, E., et al. 2010, P&SS, 58, 1555
Dobrijevic, M., Ollivier, J. L., Billebaud, F., Brillet, J., & Parisot, J. P. 2003, A&A, 398, 335
Drossart, P., Bezard, B., Atreya, S. K., et al. 1993, JGR, 98, 18803
Esposito, L. W., Barth, C. A., Colwell, J. E., et al. 2004, SSRv, 115, 299
Fletcher, L. N., Greathouse, T. K., Orton, G. S., et al. 2016, Icar, 278, 128
Friedson, A. J., Wong, A.-S., & Yung, Y. L. 2002, Icar, 158, 389
Greathouse, T., Gladstone, R., Versteeg, M., et al. 2021, JGRE, 126, e06954
Grodent, D. 2015, SSRv, 187, 23
Guerlet, S., Spiga, A., Delattre, H., & Fouchet, T. 2020, Icar, 351, 113935
Gustin, J., Grodent, D., Ray, L. C., et al. 2016, Icar, 268, 215
Janssen, M. A., Oswald, J. E., Brown, S. T., et al. 2017, SSRv, 213, 139
Irwin, P. G. J., Teanby, N. A., de Kok, R., et al. 2008, JQSRT, 109, 1136
Johnson, R. E., Stallard, T. S., Melin, H., Nichols, J. D., & Cowley, S. W. H. 2017, JGRA, 122, 7599
Kim, S. J., Caldwell, J., Rivolo, A. R., Wagener, R., & Orton, G. S. 1985, Icar, 64, 233
Kunde, V. G., Ade, P. A., Barney, R. D., et al. 1996, Proc. SPIE, 2803, 162
Lacis, A. A., & Oinas, V. 1991, JGR, 96, 9027
Lacy, J. H., Richter, M. J., Greathouse, T. K., Jaffe, D. T., & Zhu, Q. 2002, PASP, 114, 153
Lellouch, E., Bézard, B., Moses, J. I., et al. 2002, Icar, 159, 112
Lellouch, E., Bézard, B., Strobel, D. F., et al. 2006, Icar, 184, 478
Mauk, B. H., Clark, G., Gladstone, G. R., et al. 2020, JGRA, 125, e27699
Mauk, B. H., Haggerty, D. K., Paranicas, C., et al. 2018, GeoRL, 45, 1277
McEntee, S. C., Jackman, C. M., Weigt, D. M., et al. 2023, JGRA, 128, e2023JA031901
Moses, J. I., & Poppe, A. R. 2017, Icar, 297, 33
Parkinson, C. D., Stewart, A. I. F., Wong, A. S., Yung, Y. L., & Ajello, J. M. 2006, JGRE, 111, E02002
Press, W. H., Teukolsky, S. A., Vetterling, W. T., & Flannery, B. P. 1992, Numerical Recipes in FORTRAN. The Art of Scientific Computing (Cambridge: Cambridge Univ. Press)
Richter, M. J., DeWitt, C. N., McKelvey, M., et al. 2018, JAI, 07, 1840013
Rieke, G. H., Wright, G. S., Böker, T., et al. 2015, PASP, 127, 584
Rodrìguez-Ovalle, P., Fouchet, T., Guerlet, S., et al. 2024, JGRE, 129, e2024JE008299
Sinclair, J. A., Greathouse, T. K., Giles, R. S., et al. 2020, PSJ, 1, 85
Sinclair, J. A., Greathouse, T. K., Giles, R. S., et al. 2023, PSJ, 4, 76
Sinclair, J. A., Orton, G. S., Fernandes, J., et al. 2019, NatAs, 3, 607
Sinclair, J. A., Orton, G. S., Greathouse, T. K., et al. 2017a, GeoRL, 44, 5345
Sinclair, J. A., Orton, G. S., Greathouse, T. K., et al. 2017b, Icar, 292, 182
Sinclair, J. A., Orton, G. S., Greathouse, T. K., et al. 2018, Icar, 300, 305
Temi, P., Hoffman, D., Ennico, K., & Le, J. 2018, JAI, 07, 1840011
Waite, J. H., Lewis, W. S., Kasprzak, W. T., et al. 2004, SSRv, 114, 113
Wong, A.-S., Lee, A. Y. T., Yung, Y. L., & Ajello, J. M. 2000, ApJL, 534, L215
Wong, A.-S., Yung, Y. L., & Friedson, A. J. 2003, GeoRL, 30, 1447
Xu, W., Marshall, R. A., Fang, X., Turunen, E., & Kero, A. 2018, GeoRL, 45, 1167
Yates, J., Achilleos, N., & Guio, P. 2014, P&SS, 91, 27
Zhang, X., West, R. A., Irwin, P. G. J., Nixon, C. A., & Yung, Y. L. 2015, NatCo, 6, 10231